Acta Biomaterialia 118 (2020) 161–181

Contents lists available at ScienceDirect

Acta Biomaterialia

journal homepage: www.elsevier.com/locate/actbio

On the gular sac tissue of the brown pelican: Structural characterization and mechanical properties

Seth Dike[a], Wen Yang[b,c,*], Andrei Pissarenko[a], Haocheng Quan[a], Fabio C. Garcia Filho[d], Robert O. Ritchie[c,e], Marc A. Meyers[b,d,*]

[a] Materials Science and Engineering Program, University of California, San Diego, CA 92093, United States
[b] Department of NanoEngineering, University of California San Diego, CA, 92093, United States
[c] Materials Sciences Division, Lawrence Berkeley National Laboratory, Berkeley, CA 94720, United States
[d] Department of Mechanical Aerospace and Engineering, University of California San Diego, CA, 92093, United States
[e] Department of Materials Science and Engineering, University of California, Berkeley, CA 94720, United States

ARTICLE INFO

Article history:
Received 18 April 2020
Revised 6 October 2020
Accepted 7 October 2020
Available online 10 October 2020

Keywords:
Pelican pouch
Collagen
Skin
High extensibility
Mechanical properties
Constitutive modeling

ABSTRACT

The brown pelican (*Pelecanus occidentalis*) wields one of the largest bills of any bird and is distinguished by the deployable throat pouch of extensible tissue used to capture prey. Here we report on mechanical properties and microstructure of the pouch skin. It exhibits significant anisotropy, with the transverse direction having maximum nominal tensile strains of 200% to 300%, triple the value in the longitudinal direction. This is a higher extensibility than most conventional skin and is the result of the requirement of the sac to net fish; it should expand laterally, with controlled longitudinal stretch. Transmission electron microscopy provides microstructural evidence of the directionality of the collagen fibers and reveals the individual collagen fibrils with a bimodal diameter distribution having peaks at 100 and 170 nm. These dimensions are similar to collagen in mammal skin. In the lateral direction, the fibers form a curvy pattern with a radius of approximately 2 μm wherein the fibrils reorient, straighten, slide, and stretch elastically under tensile load. A second mechanism operates in the transverse direction; the membrane forms a corrugated pattern that, upon straightening of collagen fibrils, confers additional extensibility. This elicits the anisotropic response observed in tensile testing. This work focuses on the mechanical characterization based on the effect of relative bird age, sample location on the pouch, and strain rate. Anterior-posterior location and strain rate are not major influencers on exhibited strengths and extensibilities. However, bird age and dorsal-ventral location are found to affect the mechanical response of the pouch significantly. A physically-based constitutive model is developed for the middle layer of the gular sac, based on observations, which predicts maximum stresses, strains, and the shape of the stress-strain curve consistent with the experimental results.

Statement of significance

The pouch of the pelican, which is used to capture its prey, represents a superlative design by Nature in that it possess remarkable stretchablility and damage tolerance. We find that this results from the marked curvature of the collagen fibrils from which it is composed, which induces numerous energy-absorbing mechanisms where the fibrils reorient, straighten, slide, and stretch elastically under tensile load. The damage-tolerance is further enhanced by the natural gradient in its structure and properties between the pelican's beak and its pouch.

1. Introduction

The pelican gular sac is a biological material with unique extensibility, enabled by both the microstructural organization of the collagen and the corrugated architecture of the material. In a classic example of convergent evolution, a similar functional and structural property is found in the ventral groove blubber of the rorqual whale [1]. Fig. 1 shows two animals, the brown pelican and whale, belonging to different species, but possessing a similar frontal ven-

* Corresponding authors.
E-mail addresses: wyang8207@gmail.com (W. Yang), mameyers@ucsd.edu (M.A. Meyers).

https://doi.org/10.1016/j.actbio.2020.10.008
1742-7061/

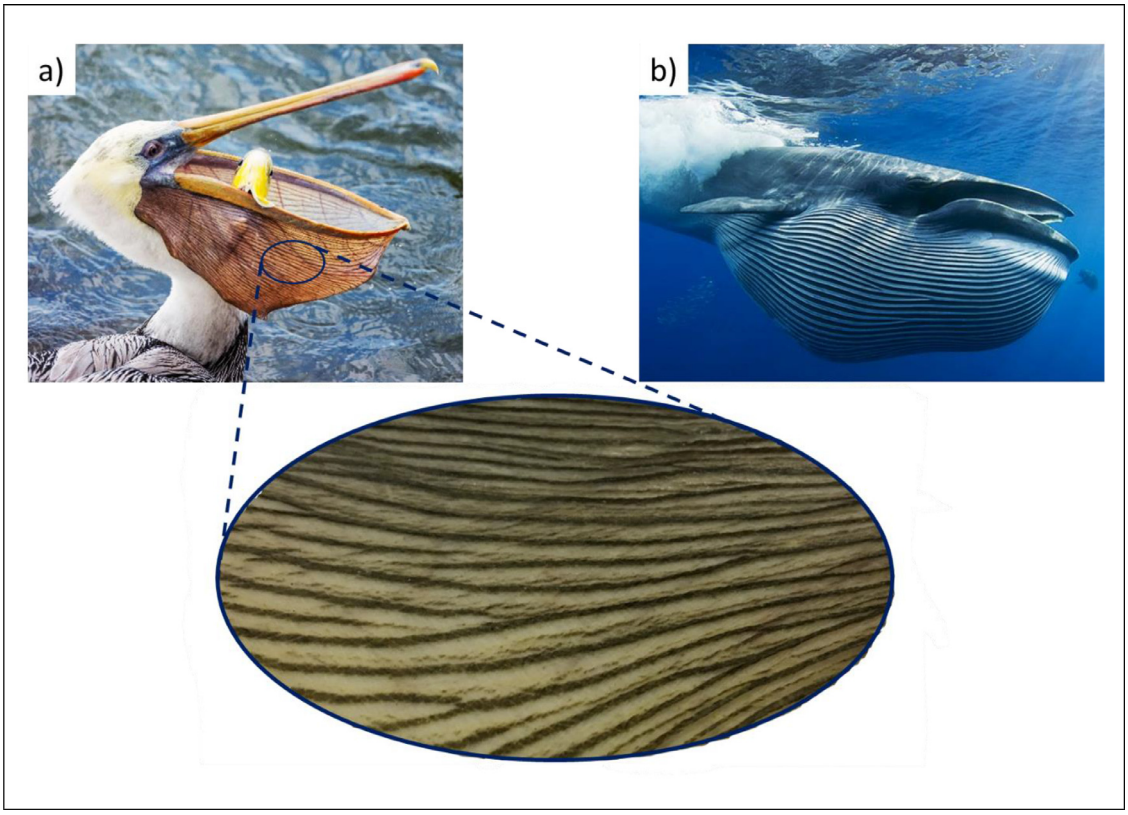

Fig. 1. Convergent evolution governed by similar feeding mechanics. (a) Gular sac of Brown Pelican (Pelecanus occidentalis). (b) Ventral groove blubber (VGB) of rorqual whales (Balaenopteridae).

tral structure, which results from the peculiar strategy of capturing prey [2]. The structures are evident and result in a high anisotropy of extensibility, a necessary requirement for capturing prey underwater.

Field et al. [1] were the first to determine the mechanical properties of the gular sac, characterizing the material for its resistance to hydrodynamic loading and pressures experienced in “dredging” for prey. Potvin et al. [3] reported that the rorquals’ ventral groove blubber was an intermediate muscle sandwiched between collagen layers. This central muscle tier is thought to limit the rate of pouch expansion, providing some extent of control to water level in the pouch. Field et al. [1] suggested that the gular sac tissue was similar in structure and that the elastic properties exhibited are defined by the behavior of collagen fibers.

Using a bubble inflation technique pioneered by Reuge et al. [4], the central sac region was tested biaxially in the form of 50 mm aperture samples over multiple inflation pressures. Field et al. [1] claimed that the material was anisotropic but based their conclusion on four tensile stress-strain curves: two from samples in the longitudinal direction parallel to the groove lines, two in the transverse perpendicular to the groove line direction. While these experiments appear almost identical for each orientation, there is simply not sufficient information to quantitatively define the properties of the gular sac. Thus, here we investigate the relationship between structure and mechanical behavior of pelican gular sac and quantitively examine the mechanisms underlying its remarkable extension.

2. Methods and materials

2.1. Sample preparation for tension tests

Pelican pouches were acquired from two sources. The San Diego Natural History Museum provided the first pelican carcass: a recently deceased specimen of mature age, or elder of at least three years. Six pelicans were released from SeaWorld - San Diego. From this set of birds, two qualified as juveniles, less than a year old, three as adolescent, between one and three years old, and one as mature. These were identified through the plumage by collaborators at SeaWorld. With the increase in age, the grooves on the pouch’s exterior become more prominent and their coloration, which begins from mossy green, saturates into a near black shade. The obtained carcasses were stored in a freezer for a few days, then thawed at room temperature for sample preparation.

The process of preparing tensile specimens began with removal of the pouch’s sample space from its attachment along the lower neck and beak. To investigate the stress and strain distribution in the pouch, samples were selected from consecutive regions defined across the length and depth, in both longitudinal and transverse directions. Occasional misting with DI water helped to keep the hydration level of the skin. Fig. 2 illustrates the extracted gular sac and the process of preparing tensile specimens at two orientations with respect to the beak axis. Each pouch provided between 24 and 30 hand-crafted dog-bone shaped tensile specimens. The dimensions of each entire dog-bone sample were 44 mm in length, 20 mm in wide and 1 mm in thickness, which left the section under test with dimensions of 14 $\times$ 8 $\times$ 1 mm, since the edges of the dog-bone shaped sample were gripped inside the fixture. The gular tissue was too tough to cut using a cutting die so the dog-bone profile was manually measured out, clamped, and sliced using a surgical scalpel. To ensure that the samples were tested in the same environmental condition, preparation and testing were completed as soon as possible, within one day. To reduce skin slippage from the gripping jaws during tensile testing, the wider ends of the dog-bone shaped samples were wrapped around a pair of toothpicks and glued with Loctite 495 adhesive which later were mounted together in the Instron for testing.

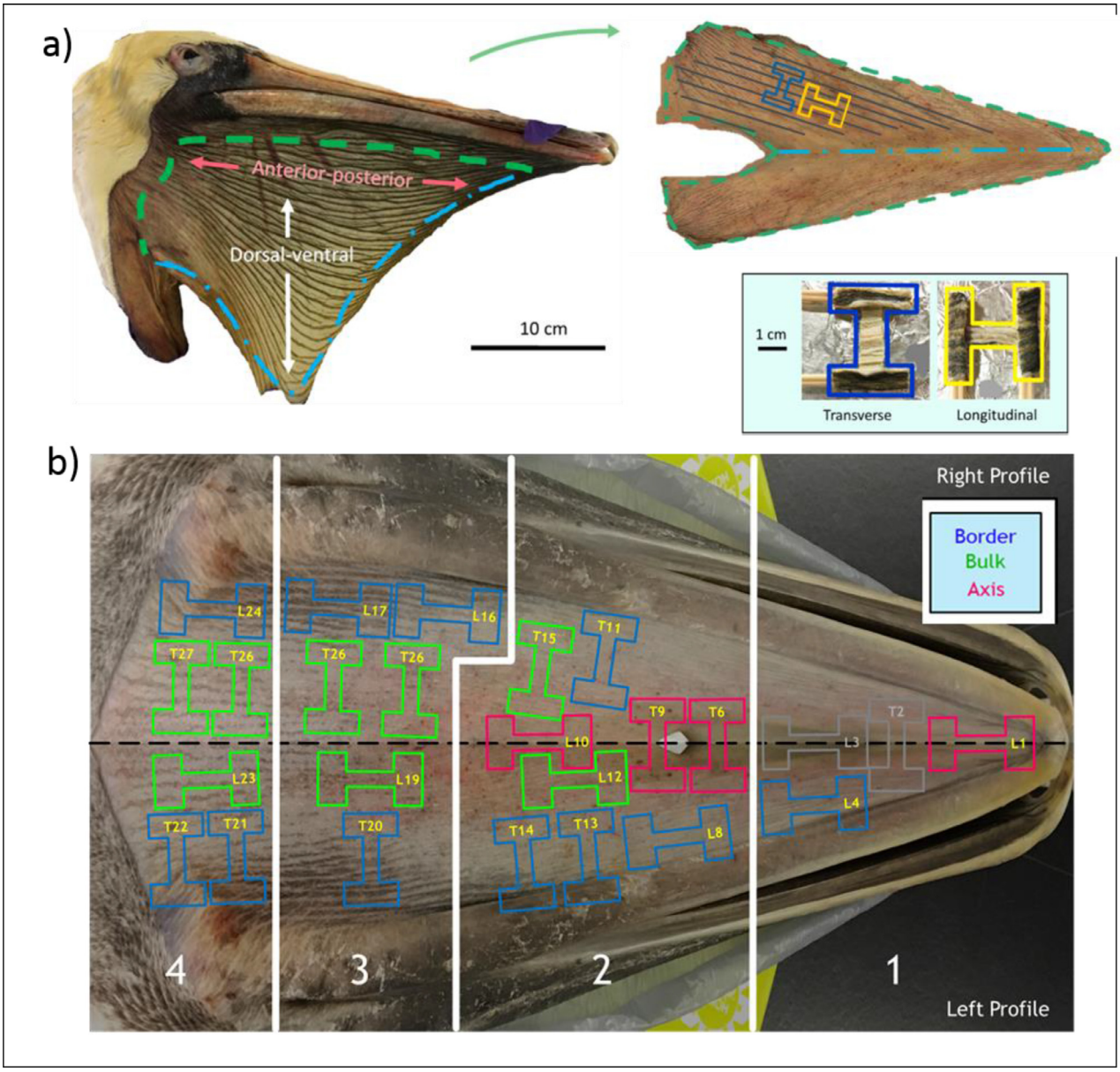

Fig. 2. Schematic illustration of our sample preparation procedures for mechanical testing. (a) Left: area used for mechanical testing. Right: extracted gular sac with transverse and longitudinal tensile specimens. Pigmented grooves run parallel to the tensile axis for longitudinal and perpendicular to testing for transverse samples. (b) Layer of gular sac with specimens (both longitudinal and transverse), extracted from three regions: along the axis, in the bulk, and along the border with the bony edge.

Uniaxial tensile tests were performed using an Instron 3342 mechanical testing machine (Instron Corp.) equipped with a 500 N load cell. Specimens were stretched at strain rates of 10^{-3}, 10^{-2}, and 10^{-1} s^{-1}, spanning two orders of magnitude. For all shown stress-strain data, the cross-sectional area was defined from the gage width and thickness of the dog-bone sample prior to deformation. The fractured samples were further treated for scanning electron microscopy (SEM) characterization.

2.2. Structural characterization of original and fractured samples

2.2.1. Ultra-high resolution scanning electron microscopy

Skin samples were cut in longitudinal and transverse orientations, with some fractured in liquid nitrogen. Sections of skin samples after excision or testing were immersed in 2.5% glutaraldehyde for 3 h to fix the structure. Samples were dehydrated by consecutive immersion in 30%, 50%, 70%, 90%, 95% and 100% (twice) ethanol solutions. The samples were then dried in a critical point dryer (Tousimis Auto Samdri 815A), and sputter coated with iridium (Emitech K575X). A FEI SFEG ultra-high resolution SEM was used to perform the characterization.

2.2.2. Transmission electron microscopy

Strips of skin for transmission electron microscopy (TEM) were taken from a freshly thawed pelican pouch. Detailed information is provided in the Supplementary Materials. Strips were incubated for 10 min in a pre-fixative and then left overnight at a temperature of 4 °C. After the fixative was removed, they underwent a series of washes, using cacodylate buffer and 3 mM $CaCl_2$ (pH 7.4) solution. Subsequently, the tissue was soaked in a mixed solution of 1% aqueous osmium tetroxide, 0.15 M cacodylate buffer, 3 mM $CaCl_2$, and 0.8% potassium ferrocyanide. This post-fixative was replaced with double-distilled water, through a 5 × 15 min series of washes while resting in ice. Samples were later incubated overnight in 2% aqueous uranyl acetate and placed in a dark environment at 4 °C. After five additional 15-minute washes, the tissue was dehydrated

through an ascending ethanol series, at 20%, 50%, 70%, 90%, and 100% solutions rested in ice. This was followed by two 100% dry ethanol washes and one wash at a 1:1 ratio of acetone and ethanol at room temperature, and finally the sample was preserved in the 100% acetone overnight. The fully dehydrated specimens were embedded in increasingly concentrated Durcupan ACM mixtures and polymerized in the pure resin at 60 °C for 48 h. The solidified samples were sectioned parallel to the exposed skin surface, using a Leica Ultracut UCT ultramicrotome and Diatome diamond knife to produce thin films of 70–100 nm thickness. Sections were set on TEM copper grids and finished with Sato lead staining.

TEM images were taken on FEI Technai 12 (Spirit, 120-kV) TEM (FEI, Hillsboro, OR). The image recognition software Fiji [5] was used for all image post-processing.

2.3. Statistical analysis

The JMP statistical software package [6] was used to perform multiple regression analyses to assess the influence of sample orientation, location, and age (mapped by pelican sample) on the responses shown in the Supplementary Materials section, namely heel slope, heel intercept, linear slope, linear intercept, maximum stress, strain at maximum stress, and strain energy. Multiple analysis of variance (MANOVA) data results and scatter plots of these data are also given in Figures S1-S4.

3. Results and discussion

The characterization of the structure, from meso– to nano-levels, enables an understanding of the toughening mechanisms. The pelican pouch presents an extremely anisotropic response due to the unfolding of the skin in the transverse direction, experiencing high strain at a low load until the corrugated cross-section is flattened. Knowledge of rorqual whale ventral groove blubber further supports this unusual mechanism; this tissue has been reported to extend up to 400% of its original length in the circumferential direction [7].

3.1. Hierarchical structural characterization

Initial understanding of the pelican skin's hierarchy begins with a three-layer structure, depicted by Williams et al. [8], which shows the skeletal muscle to be sandwiched between specialized epidermal layers, as shown in Fig. 3. The epidermis is defined specifically as stratified squamous epithelium. The 'stratified' descriptor attests to the arrangement of cells as a multitude of layers as 'squamous' ones consisting of flattened cells. Due to the constant abrasion, the dead cells shed form the stratum corneum, or exposed epidermal surface. Fig. 3c shows the three layers observed in the gular sac. This schematic representation is at a higher magnification than that of Fig. 3b. The external and internal layers show an obvious wavy curvature. The image solely reveals a corrugated geometry of the middle layer, created by folding the external surfaces. This transverse specimen image is redrawn at a higher magnification in Fig. 3c with the three layers clearly shown and the outside layer displaying melanocytes.

The sequence in Fig. 4a illustrates how the corrugated structures (in green) shift, unfold, align, and stretch in the process of rectification, responding to loading. The detailed arrangement of the folds is shown in Fig. 4b; it shows the structure of the pocket, divided into the horn and wall during the unfolding process. The form resembles an "M" shape. Once the middle collagen layer (in red) is extended, the response mainly relies on the mechanical behavior of collagen fibers. This is analyzed in Sections 3.4–3.6. An optical micrograph of a specimen stretched in tension reveals that the folds are removed with only a linear aligned structure remaining.

Fig. 5a presents an overview of the cross-section of the pelican pouch. It is clear that the pouch skin contains three layers. Evidence of keratin in the pouch's exterior as well as interior is shown in Fig. 5b. Keratinous cells form thin sublayers to the stratum corneum. The thick middle layer is composed of collagen fibers (Fig. 5c). One can see the curvature of the collagen fibers (shown in Fig. 5d) which are formed from the collagen fibrils with characteristic *d*-banding (shown in Fig. 5e).

This highly curved nature of the collagen fibers provides one of the prime components responsible for its large extension. Fig. 6a depicts the representative process of estimating the fibril curvatures. The circular regions are highlighted by red circles. There are straighter segments between adjacent circular regions, generating the ability to increase the maximum strain beyond that of assemblies of semicircular segments. Curves with radii between 3 and 7 μm can be seen in the pelican skin, with few circular segments more than 8 μm in radius observed. Circular segments with smaller radii provide larger extension under tension. These are the extremities of straight segments and their opening aligns these segments creating high strain. The curved configuration of the collagen fibers in the pouch, and their specific radius of curvature, are compared in Fig. 6b with that in pig dermis [10], although in the pig dermis, the long straight segments of the collagen fibers were mostly absent.

TEM analysis confirmed the extreme curvature of the collagen fibrils in both the longitudinal and transverse directions. Although no picrosirius red, confocal, or second harmonic observations were made here, the tri-dimensional nature of the fiber arrangement, first determined by Bircher et al. [9] and subsequently by Annaidth et al. [11], Meador et al. [12], and Rezakhaniha et al. [13], is confirmed; indeed, a similar tri-dimensional structure was found for porcine skin [14]. Fig. 7 shows the arrangement of these fibrils in a transverse section. There is considerable curvature in the fibers, which typically have a diameter of ~2 μm, indicative of the large extensibility in the transverse direction. This is the classic hierarchy of collagen in the dermis. However, in the present case, the folding of the fibrils is more extreme than in the pig dermis. The circular regions are not restricted to the foil plane, but coil in and out of the plane (Fig. 7a) confirming the tri-dimensional pattern identified by Pissarenko et al. [14]. The longitudinal section shows fibers that tend to be less curvy and more aligned with the axis of the sac, as shown in Fig. 8a; the boundary between these two orientations of collagen is indicated by the arrow this figure. The collagen fibrils can be seen in orientations parallel, inclined (squares), and normal (circles) to the foil. The diameter of collagen fibrils, observed in the TEM images, ranged from 50 nm to 220 nm (Fig. 9a). Their distribution in Fig. 9b is bimodal, with two maxima in fibril diameters at 102 nm and 171 nm.

Table 1 lists the measured fibril and fiber sizes, by comparison to the data extracted for a 9-month old female pig [10] and female rabbit [15,16] dermis. In terms of the fiber thickness, the collagen fibers in rabbit skin average between 1 and 2 μm; note these were measured from the fibers running parallel with foil plane. For pig skin, the average thickness of collagen fiber was 2.2 μm. Current measurements for the pelican pouch are 2 to 3 μm. As these values are relatively similar for all animals, the fiber thickness does not appear to be a prominent parameter causing the skin's exceptional extensibility.

Rabbit fibrils displayed diameters that were between 50 and 100 nm [16]. Values for the pig fibrils were measured normal to the image with a peak in the fibril diameter distributions at 82 nm and a secondary peak at 112 nm. This compares with the peaks in fibril diameter distributions for the pelican, which are 102 and 171 nm (Fig. 9b). Despite the variance observed in the distribu-

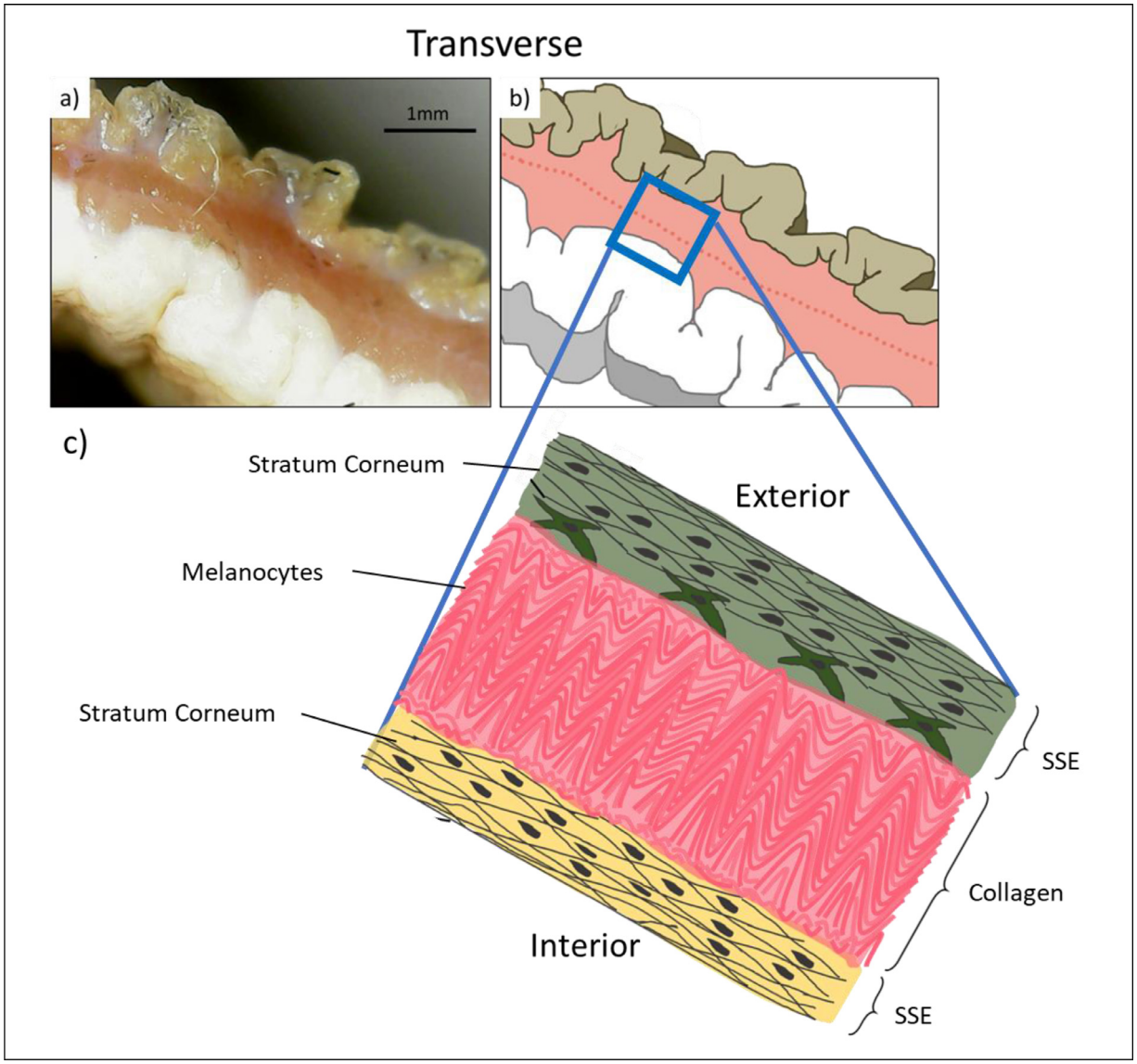

Fig. 3. Crimped structure of gular sac. (a, b) Macroscopic crimping along the gage length of the transverse section; (c) Schematic representation of a magnified view of the section through the gular sac tissue parallel to the pigmented grooves containing melanocytes. The inner layer of collagen consists of oriented fibers, with shorter and smoother coiling bordering the dermal outskirts. (SSE = stratified squamous epithelium).

Table 1
Comparative values in the fibril and fiber microstructures for the pig, rabbit, and pelican. Note our values are based on a bimodal distribution where the first peak is dominant (see Fig. 8).

Parameter	Direction fibers/fibrils run to foil:	Pelican	Pig	Rabbit
Fiber Thickness (μm)	Parallel	2–3	2.2	1–2
Fibril Diameter (nm)	Parallel	127.7, 178.3	–	50–100
Fibril Diameter (nm)	Normal	102.1, 170.6	82, ~112	–

Source: Nine-month-old female pig belly skin [10]. Female rabbit skin [15,16].

tion's tail (~170 nm), fibril diameters can be broadly considered similar in these three animals (~100 nm): rabbit, pig, and pelican. Fibril diameter in the dermis is thus also not likely to be a prominent factor in generating the additional extensibility observed in the pelican gular sac relative to regular skin. It has been observed for tendons and ligaments that strenuous exercise can increase the fibril diameter [17]. According to Herod et al. [18], the fibril diameter in the tendons also varies at different locations and with different function (*e.g.*, for extensors vs. flexors) from 70 to 160 nm (where the extensors tend to have thicker fibrils than the flexors). Thus, the varying distribution of fibril diameters might be the result of prior exertion, in addition to their location on, and function of, the gular sac.

3.2. Effect of age on anisotropy

The foraging success of the brown pelican as a function of age and height of dive has been studied by Arnqvist [19]. Surprisingly,

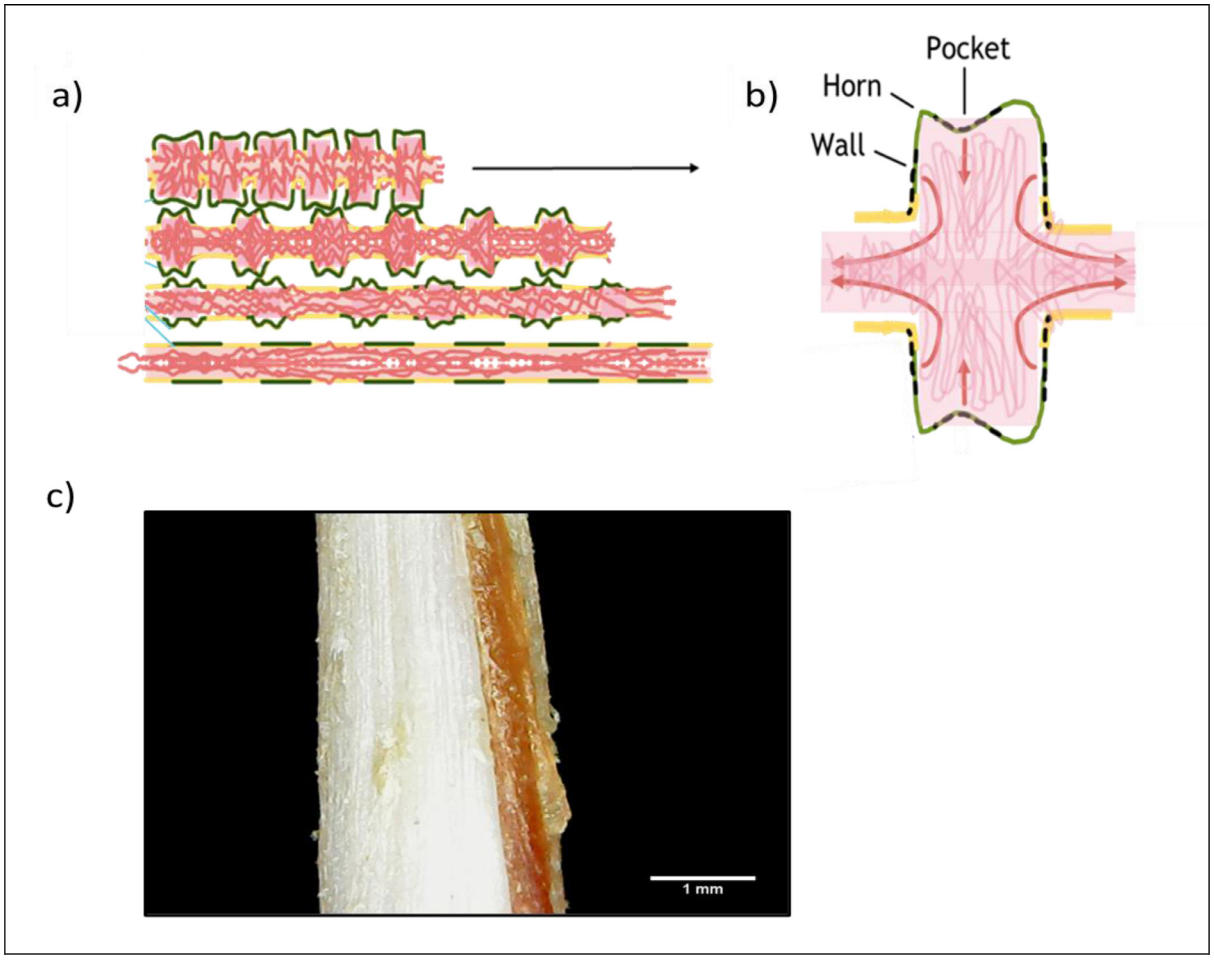

Fig. 4. Reversible process of unfolding(a, b) Sequence of extension by rotation of wall and pocket components of the 'M' to align with tensile axis. Once the structure has been unfolded, the sac can stretch as a single entity. (c) Optical micrograph of sac after complete stretching until straightening of the 'M' pattern.

although the adult pelican has a higher success rate in capturing food, both adults and juveniles show the same handling time in the pouch. It is of interest to study how age may affect the mechanical behavior of the pelican pouch. Fig. 10a shows the characteristic J-shaped tensile stress vs. strain response of skin due to the behavior of the collagen fibrils and the interaction between the collagen and matrix (also called ground substance) in skin [15], consisting of the toe, heel, and linear regions which precede failure. According to Yang et al. [15], in the toe and heel regions the collagen fibrils straighten and rotate with some degree of stretching toward the tension direction, whereas in the linear region, the fibrils undergo realignment, rotation, elastic stretching, and sliding; these are illustrated schematically by the inserts in Fig. 10a up to fracture. The tests in which the specimens did not undergo instantaneous failure were stopped at the maximum stress because subsequent deformation occurred with large geometry changes where the stresses could not be readily interpreted.

Figs. 10b,c show the engineering (nominal) stress-strain plots for the pouches of juvenile and mature birds, respectively. There is significant overlap in the stress-strain response in longitudinal and transverse directions of the juvenile pelican pouch (Fig. 10b) although some of the curves obtained in longitudinal direction exhibit much lower maximum strains. The pouches of mature pelicans display curves that are quite anisotropic. Samples in longitudinal direction tend to exhibit a higher strength and lower maximum strain. In these samples the grooving of the sac was aligned with the direction of applied stress, as shown by the anterior-posterior direction in Fig. 2, *i.e.*, the rectification of the corrugated structure, as shown in Fig. 4, does not take place. As such, these longitudinal samples display a lower failure strain.

Transverse samples exhibit lower maximum nominal stresses and, conversely, higher strains. However, these are not true values as they are based on the initial cross-sectional area. Using average maximum strains in the longitudinal and transverse sections of 1.5 and 3.5, one can calculate the ratio of the maximum engineering stresses based on equal true stresses. This conversion assumes a Poisson's ratio of 0.5 (constant volume). If the two maximum true stresses are the same, one obtains a ratio between the engineering stresses in longitudinal and transverse directions of 1.8. Average values of the maximum stresses from Fig. 10c are $\sigma_l = 7$ MPa for the samples in longitudinal direction and $\sigma_t = 4$ MPa in transverse direction; the ratio of the longitudinal to transverse stresses, σ_l/σ_t, is equal to 1.75. This is consistent with the ratio of 1.8 calculated based on the same maximum true stress.

3.3. Gradient in mechanical response

As the gular sac tissue has to exhibit diverse values in mechanical properties across the pouch space for the purpose of carrying food, the strength distribution in the pouch was also investigated in both the longitudinal and transverse directions. The dorsal-ventral (transverse) direction goes from the mandible to the

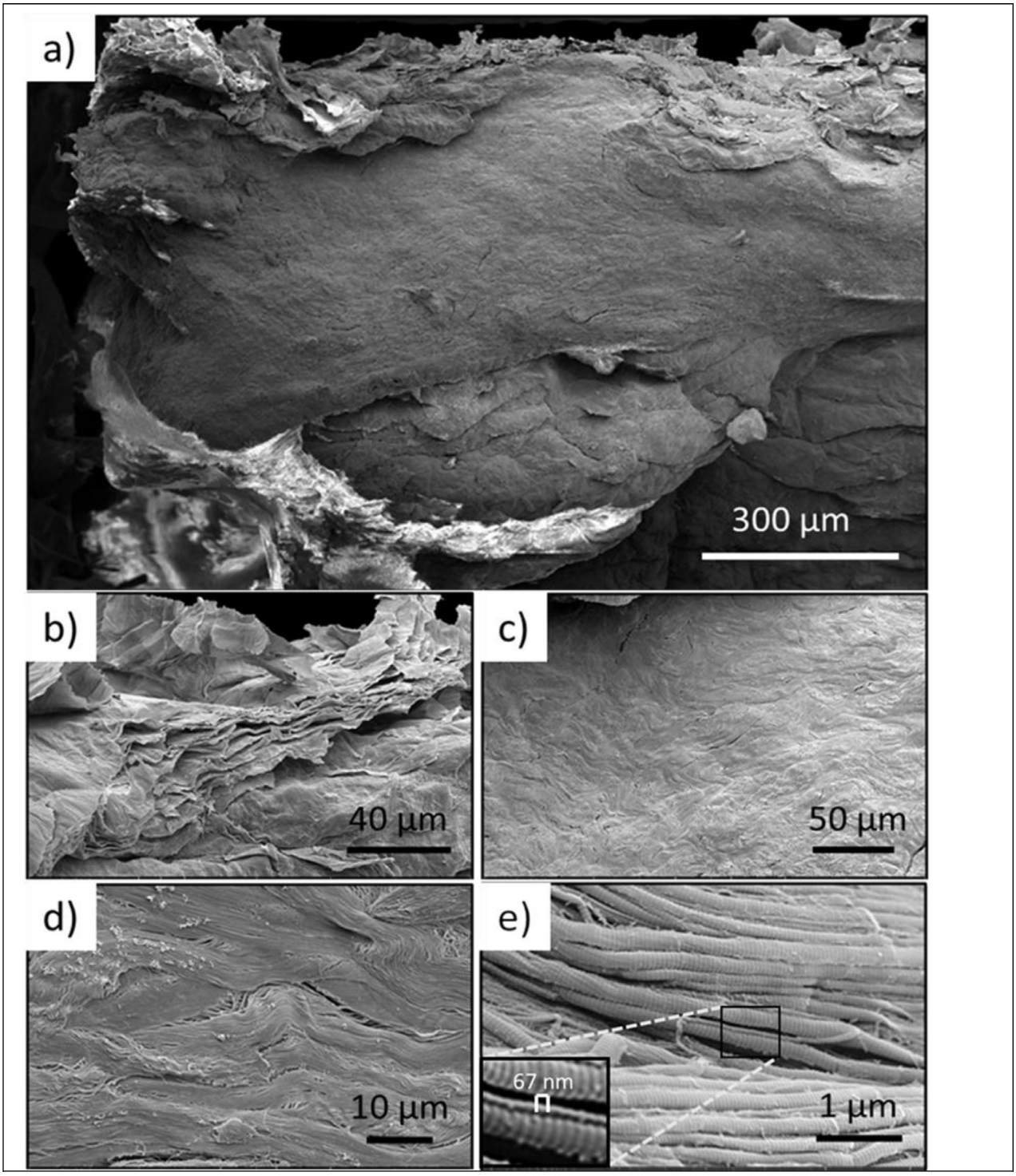

Fig. 5. Scanning electron micrographs of the gular sac tissue. (a) Overall view of the fracture surface. (b) Keratinized exterior of dermal tissue. (c-d) Bundles of collagen (fibers), shown in Fig. 7a, coil in and out of plane, forming lamellar structures. (e) Higher magnification images highlights the *d*-spacing for individual collagen fibrils with varying diameters.

belly of the pouch; the anterior-posterior (longitudinal) direction, perpendicular to the dorsoventral direction, is aligned with the length of the beak, from its anchor point in the skull to the tip as shown in Fig. 2.

3.3.1. Anterior-posterior gradient

Combined with the pelican's short neck, the pouch skin carries much load and provides extra space and high extension for the food to be swallowed down. Fig. 11 shows the division of the sac into four regions, designated 1 (closest to tip of beak), 2, 3, and 4 (closest to skull). The mechanical testing results show a gradi-

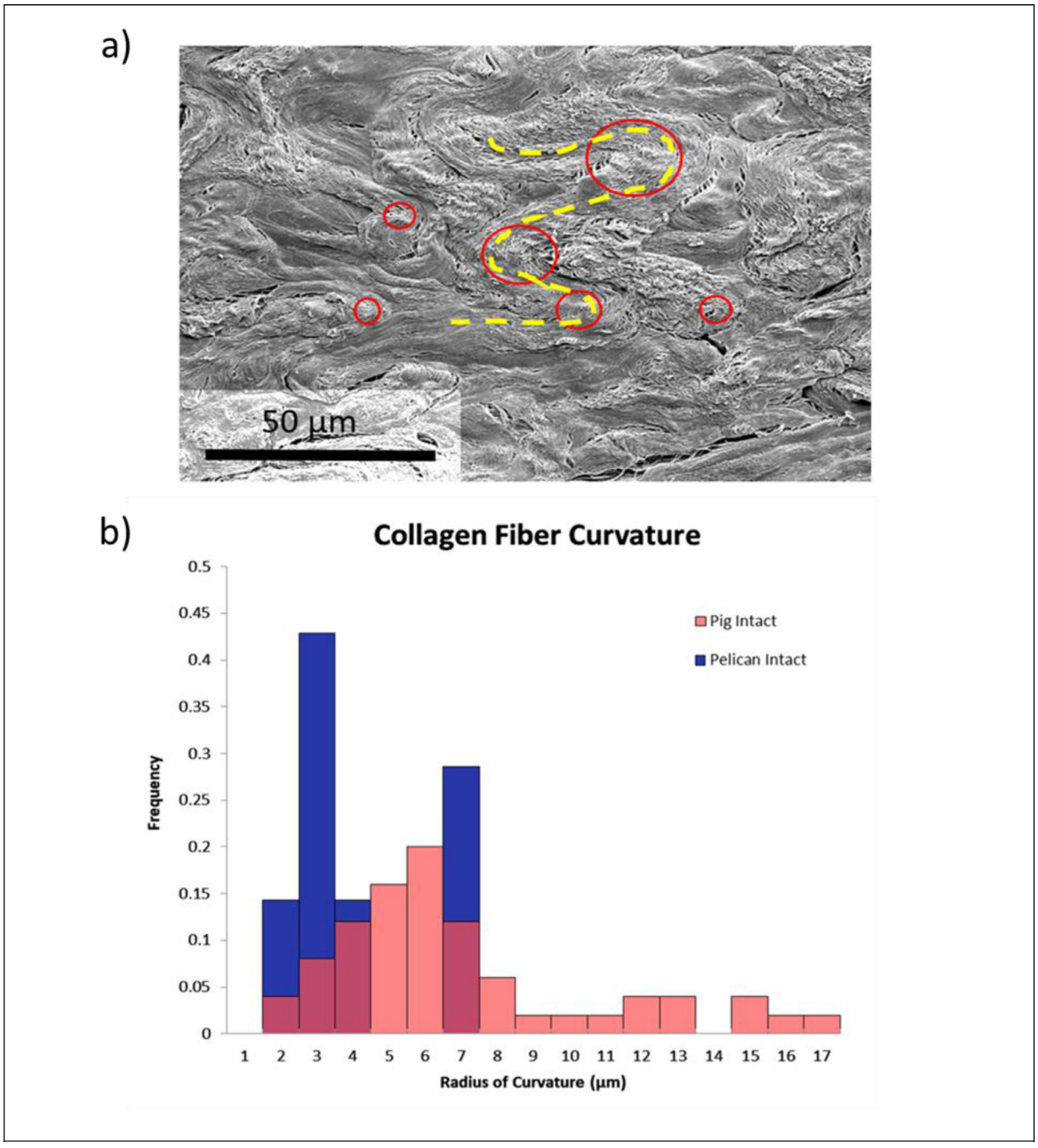

Fig. 6. a) Curved configuration of collagen fibers (longitudinal section); centers of circles marked in red. Yellow dashed lines highlights collagen configuration in a fiber; b) Distribution of radii of curvature for collagen fibers of pig and pelican gular skins. Note smaller radii and straight segments for gular sac could contribute to larger extensibility.

ent of values across these regions; in general, a higher maximum strain in Region 3 where the entire food (*i.e.*, a fish or bird) can be deposited, and a higher maximum stress at the Regions 3 and 4 since the pelican swallows the entire food down to its stomach. The mechanical gradient of the pouch in the transverse direction is more distinct than in longitudinal direction. Clearly, the function of the pouch in the transverse direction is to serve as a big "folded" bag to carry food. Visualization of the data using histograms (Figs. S1-S4) and the stress-strain curves both suggest the following trends from skull to beak tip: a decrease in maximum engineering stress, an increase in failure strain, and a decrease of the elastic modulus for heel and linear regions of the stress-strain curves.

3.3.2. Dorsal-ventral gradient

The samples were separated into three groups: border (close to beak), bulk, and axis (along the symmetry axis of pouch; see the blue dash-dotted line in Fig. 2a or the black dash line in Fig. 2b). The results are shown in Fig. 12. There is a clear gradient in the longitudinal samples; the ones close to the border are significantly stiffer, which is a reflection of the necessity for stiffness at the pouch-beak interface. Such a natural design enables the pelican to

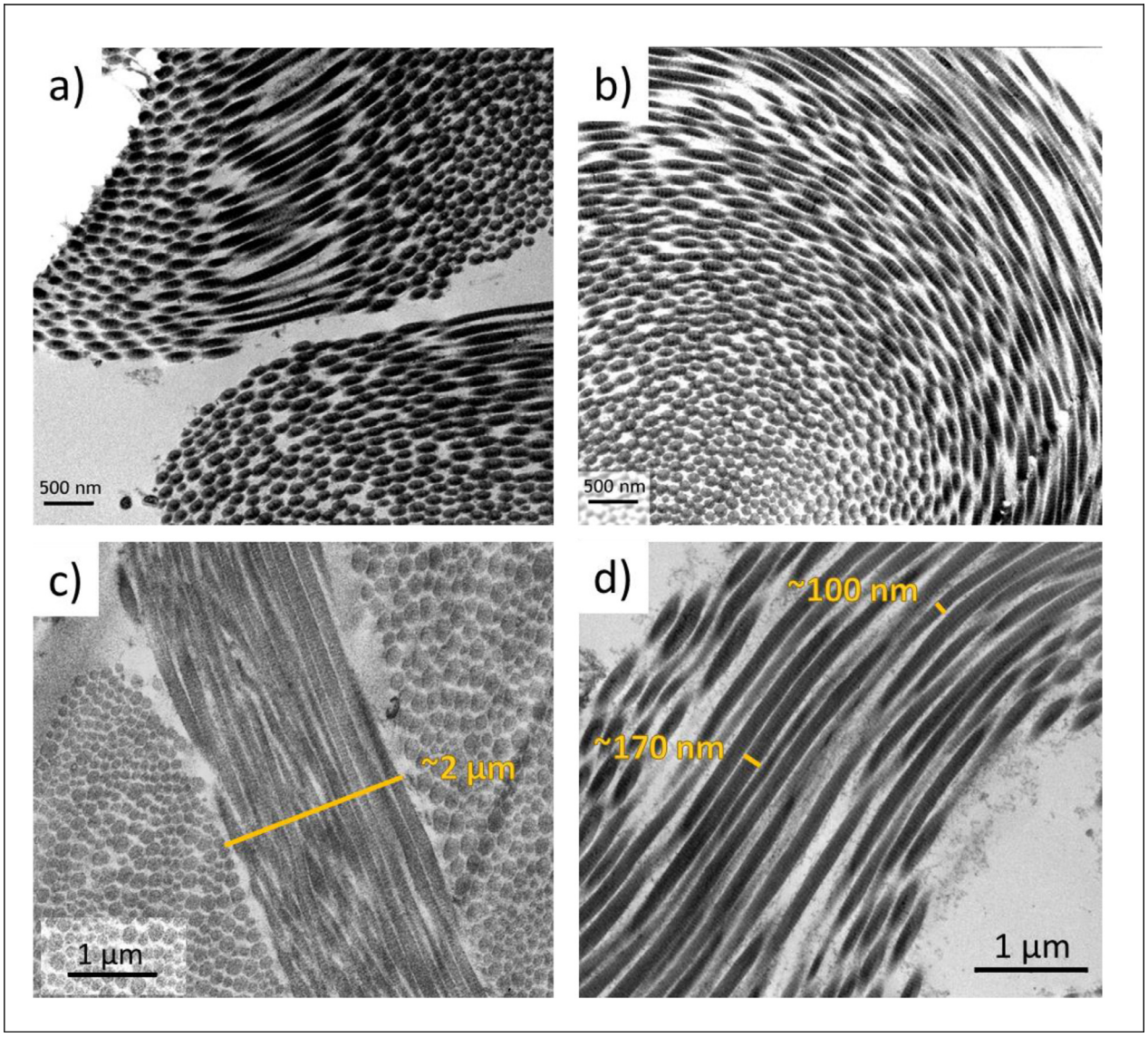

Fig. 7. Transmission electron micrographs showing the configuration of collagen fibrils imaged with foil in transverse orientation. (a) Out-of-plane coiling of fibrils which have an elliptical shape because they are sectioned at an oblique angle to their longitudinal axis. This represents the intersection of the fibrils with the foil surface. The variation in the elliptical eccentricity demonstrates the change in orientation of the fibrils. (b) In plane coiling of fibrils forming a vortex-like configuration. (c-d) Estimation of fiber thickness and fibril diameter.

carry the food and water without having the pouch fail at the beak due to a discontinuity in mechanical properties. This greater stiffness of the 'border' samples is also manifested in the transverse direction.

Further evidence of these gradients in the material response as a function of dorsal-ventral location is provided through the histograms in Fig. 13, which display the data extracted from the stress-strain curves quantified through the averages and uncertainties in each property.

The skin belonging to the 'border' region possesses significant strength because it connects to the more mineralized and hence much harder pouch rim. This represents a gradient in stiffness and strength. In contrast to this, the 'axis' region contains a thicker foundation of muscle tissue responsible for the control of pouch inflation by pulling the pouch open as water presses into it. This may help the pouch relax in a more aerodynamic form and help maintain some of the initial shape during filling. This region is capable of higher extensibility/strain than the other two regions.

3.4. MANOVA results for dorsoventral gradient

Figure S1 in the Supplementary Materials section shows the scatter plots for the slope in the heel region (as shown in Fig. 10a). The central green horizontal line in each diamond shape in Figures S1 and S2 identifies the mean value of the group while the vertical span of the diamond points represents the 95% confidence levels of the means. A multiple analysis of variance analysis (MANOVA) produces orientation and location p-values < 0.001 indicating that the mean heel slope value is strongly correlated with those factors. The p-value for age was 0.849 indicating little correlation between the mean heel slope value and the estimated age of the pelican. Grouping the bulk and axis location data provides a much clearer correlation of location with the heel slope parameter.

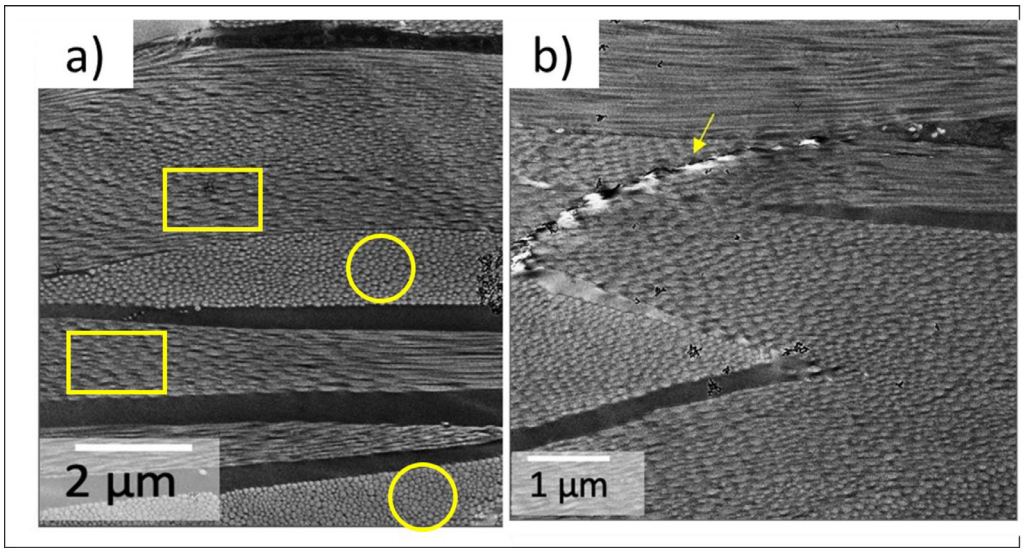

Fig. 8. Transmission electron micrographs showing the configuration of collagen fibrils imaged in longitudinal orientation. Fibers are much straighter than in transverse direction. Fibril diameters are 100–170 nm and fibril thickness ~2 µm.

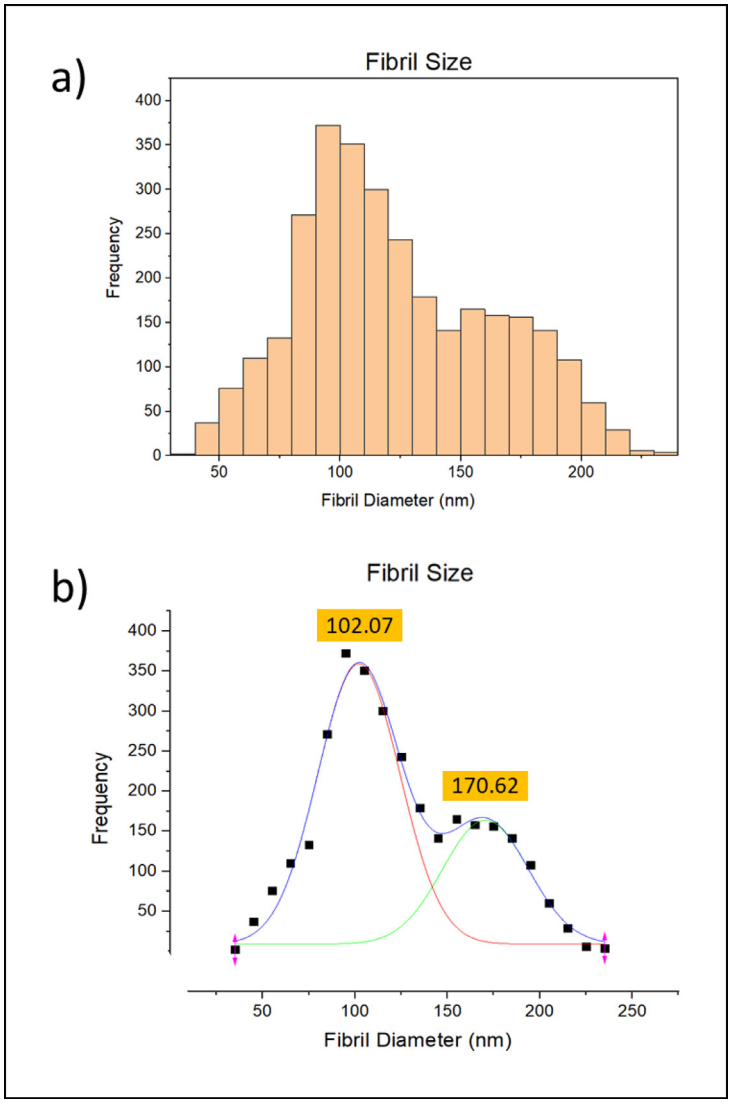

Fig. 9. (a) Distribution of over 3000 identified fibril diameters normal to the transverse section. (b) Bi-modal distribution highlighting primary and secondary peak diameters of 102 and 170 nm. The imaging software Fiji was used to distinguish individual collagen fibrils, allowing for the calculation of such dimensions.

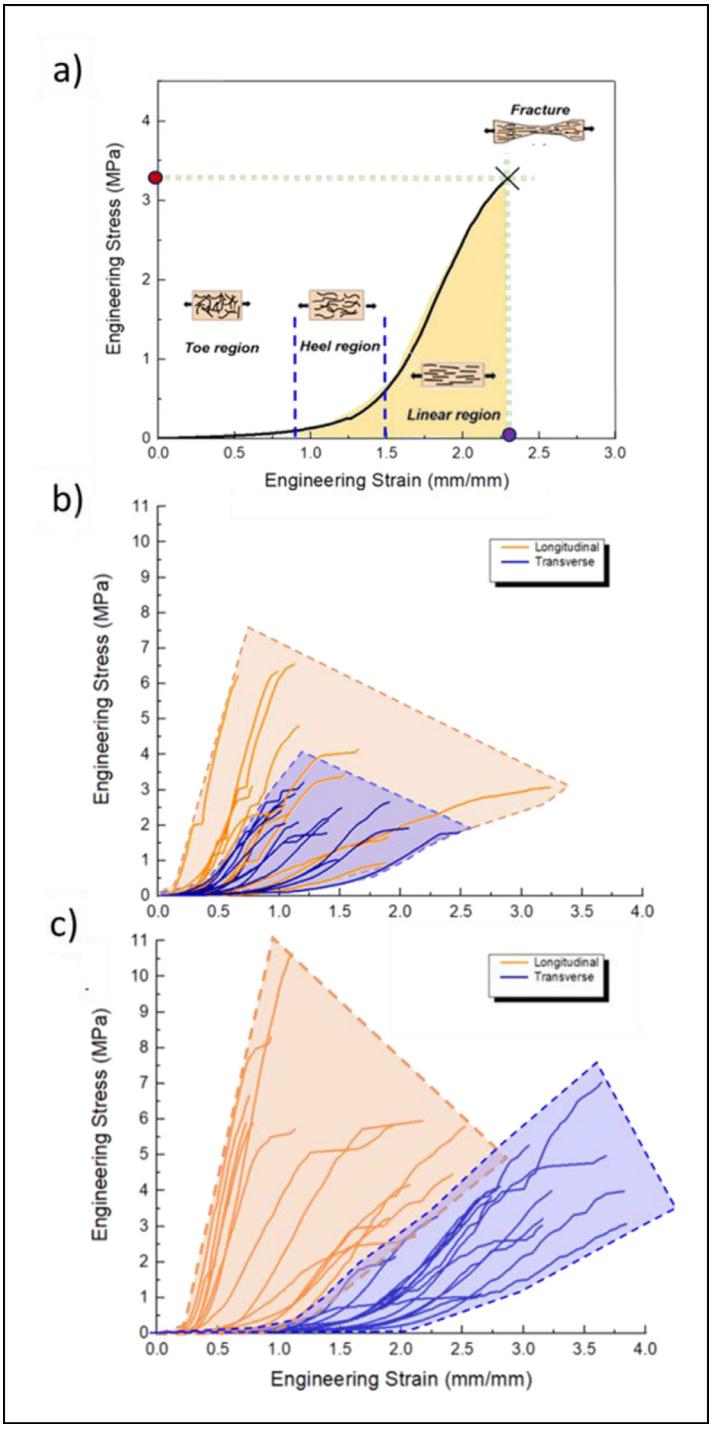

Fig. 10. (a) Four characteristic stages of the tensile response of skin: toe, heel, linear region, and, finally, failure. (b) Engineering stress-engineering strain response for a juvenile specimen. Separation by testing orientation is almost non-existent, but several longitudinal specimens exhibit very low maximum strains. (c) Engineering stress-engineering strain response of mature specimens. Distinct grouping by testing orientation and significant anisotropy. Note that the plotted stress is truncated at the maximum value recorded, where either sudden failure occurred, or the specimen failed under decreasing loads with major geometry changes such that accurate stress and strain values could not be calculated.

Scatter plots show the same data (small *p*-values) for the other factors (*e.g.*, heel intercept, linear slope, and linear intercept), with the orientation and location (border compared to axis and bulk) being strongly correlated with all response parameters.

3.5. Model of high extensibility of gular sac

A constitutive model is presented here that predicts the maximum strain in the transverse and longitudinal directions from the initial configuration of the fibers. These are only approximate

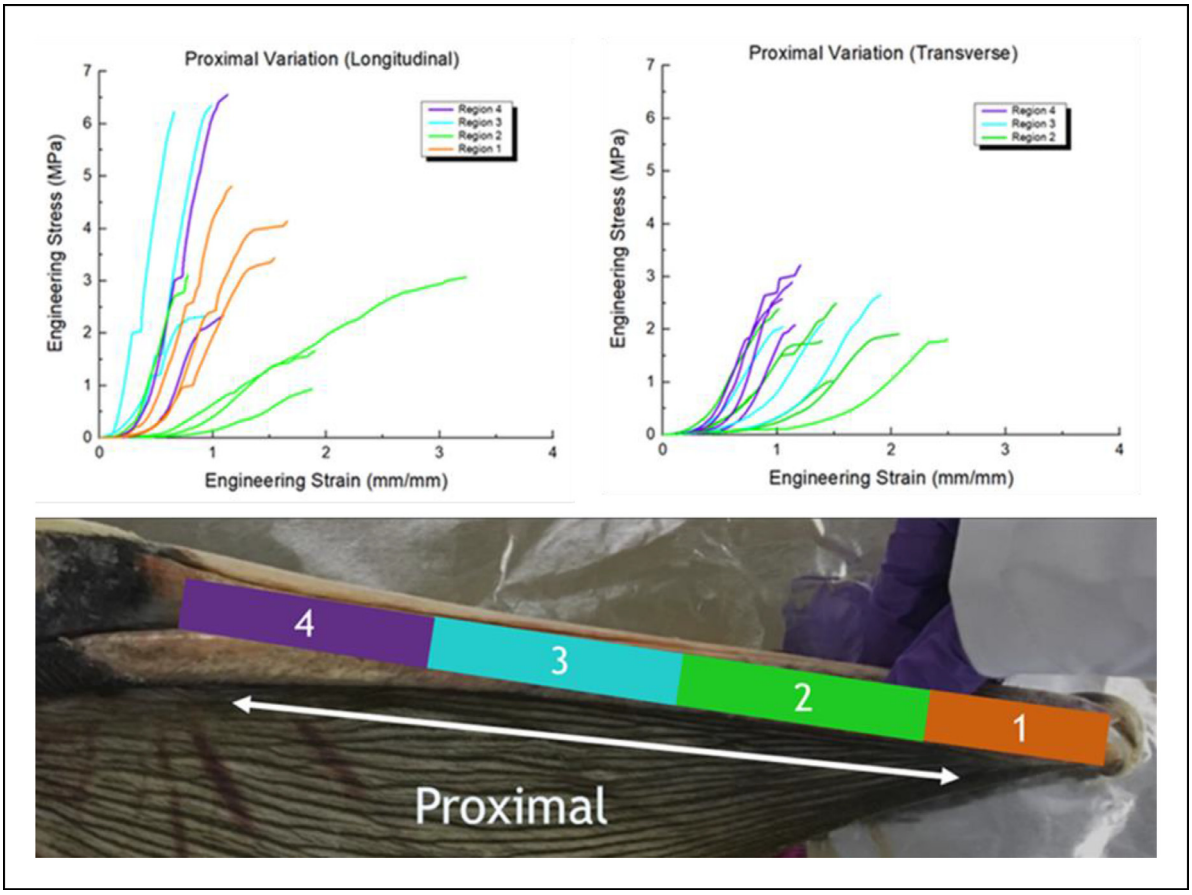

Fig. 11. Gradients in mechanical properties exhibited in the proximal direction for each testing orientation. Generally, the further back (nearest the skull) the specimen, the stiffer and stronger the skin. The exception to this statement is the tip (zone 1 in brown), whose extensibility in the longitudinal direction is limited by the closeness of the mandibles.

values, because it has been shown for both rabbit and pig skin [10,15,16] that sliding between fibrils and fibers can generate significant strains. The interfibrillar and interfiber sliding could not be quantified in our experiments and is likely to cause irreversible deformation. Focusing strictly on reversible deformations, three main mechanisms that contribute to the remarkable extensibility of the gular sac can be identified:

- collagen fiber rotation and alignment along the tensile direction.
- collagen fiber unfolding, when fibers transition from their initial wavy configuration to fully straight lines; this includes the configurational changes to the pocket, horn, and wall components of the corrugated layer (shown in Fig. 4).
- elasticity of collagen fibers, prior to relative sliding and internal delamination.

The first two processes define the configurational deformations in the inner layer. They contribute mainly in the toe and heel regions of the J-curve and can be evaluated by estimating the geometric arrangement of collagen fibers, shown in Figs. 5–7. Similarly, the configurational deformation of the interior and the exterior strata corneum can be estimated by comparing the total length of the unfolded layers with their end-to-end length in the resting configuration (the M-shaped folds), as illustrated in Fig. 4. In this case, the process of unfolding occurs at the macroscopic level, and is the only one that dictates the configurational stretch of the layer, as no realignment takes place. It mostly applies to the transverse direction, as it is the one perpendicular to the grooves. A generalized Maxwell model for the transverse direction (in Fig. 14a) is proposed, assuming a parallel arrangement of the interior stratum corneum, the middle collagenous layer, and the exterior stratum corneum. Note that a matrix component in the collagenous layer is also added in parallel to ensure that the entire structure recoils to its initial position once the loading is released; the configurational component of others is unable to spring back otherwise.

By definition, the model implies that the strains in each branch must be the same, *i.e.*, the total strain state ε_{tot} is the same in the interior *stratum corneum* (SC_{int}), the middle collagenous layer (*col*), the middle layer matrix (*mat*), and the external *stratum corneum* (SC_{ext}), such that $\varepsilon_{tot} = \varepsilon_{SCint} = \varepsilon_{col} = \varepsilon_{mat} = \varepsilon_{SCext}$. Each strain can then be subdivided into configurational (ε^{conf}), elastic (ε^{el}), and viscous contributions (ε^{η}):

$$\varepsilon_i = \varepsilon_i^{conf} + \varepsilon_i^{el} + \varepsilon_i^{\eta}, \tag{1}$$

where $i = \{SCint,\ col,\ SCext\}$. For the matrix, $\varepsilon_{mat}^{conf} = 0$. The configurational strain in each layer can also be separated into unfolding ($\varepsilon^{conf_{unfold}}$) and rotational parts ($\varepsilon^{conf_{rot}}$) with the latter only affecting the collagen in the inner layer. For each component, we measure the configurational strain related to structural unfolding as follows:

$$\varepsilon_i^{conf_{unfold}} = \frac{L_M}{L_E} - 1, \tag{2}$$

where L_M is the total length of the pocket, horn and wall of the M-shaped corrugations (in Fig. 4c-d) and L_E is the end-to-end dis-

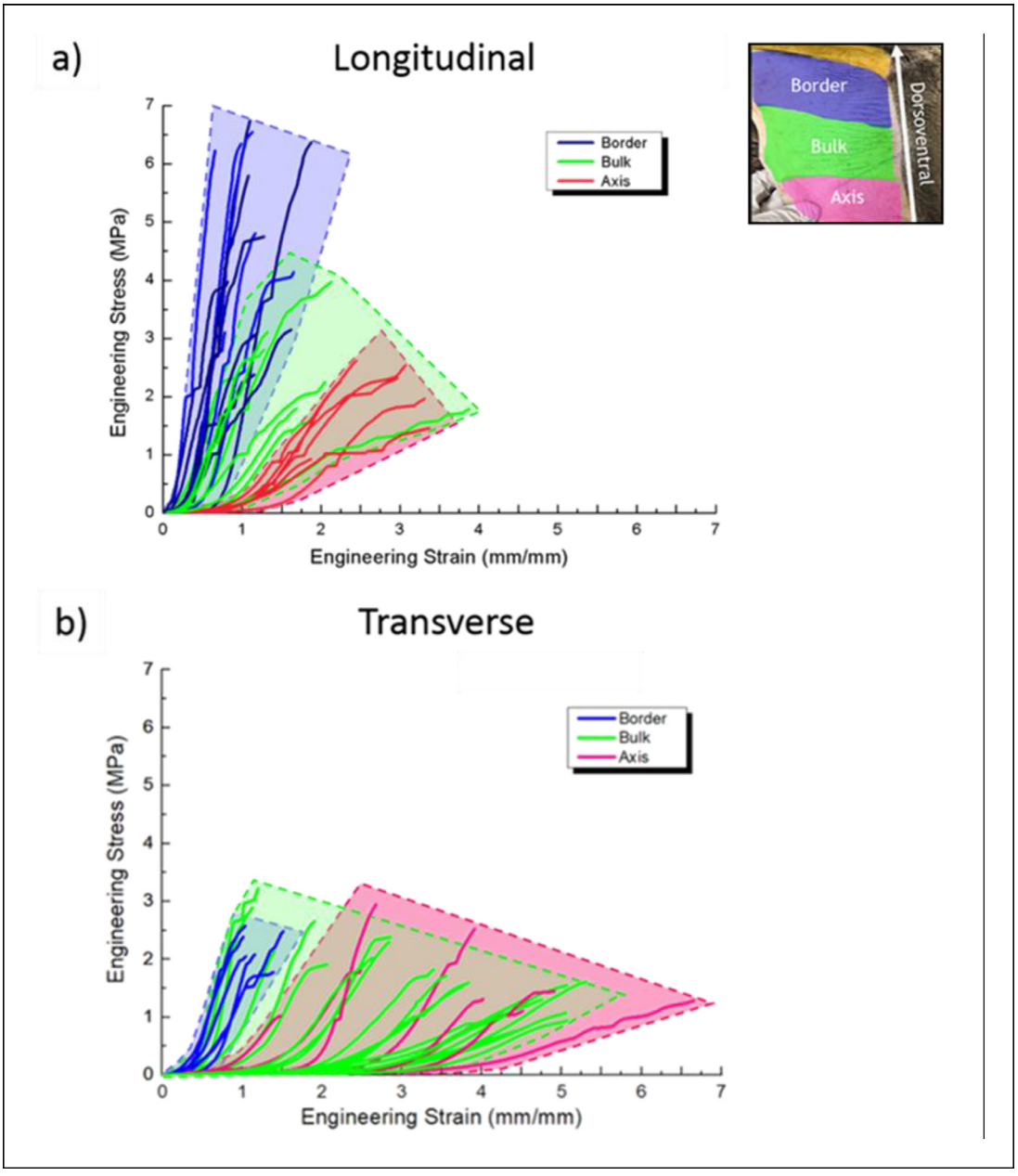

Fig. 12. Gradients in mechanical response exhibited in the dorsoventral direction for longitudinal and transverse orientations. Specimens that 'border' the beak are consistently stiffer, exhibiting lower maximum strains. This is a necessity of the boundary conditions, the beak exhibiting negligible maximum strain. (a) For the longitudinal orientation, these additionally embody high stiffness and strength properties. Although bulk and axis bands overlap to a great extent, the axis specimens are associated with properties of high strain and generally low strength. (b) The two high-strength fuchsia curves that lift the axis band are classified as both border and axis. Being of the beak tip, these specimens balance border characteristics of higher strength and stiffness with axis ones of withstanding larger strains.

tance, illustrated by the dashed pink line in Fig. 4c, for the case of the interior and exterior *stratum corneum*. For the collagen fibers, L_M corresponds to the arc length of a wavy fiber, while L_E stays the same. Both lengths are taken over a given portion of material.

Table 2 summarizes the calculated average values of $\varepsilon_i^{conf_{unfold}}$. We find that for the interior *stratum corneum*, the middle collagen layer, and the exterior *stratum corneum*, the estimated unfolding strains are respectively 0.68±0.01, 1.07 ± 0.14, and 0.84 ± 0.13; these calculated values and their maximum (1.07) are much higher than those for rabbit and pig skin (which are ~0.06–0.1) [10,15,16]. Note that this calculation does not include the elastic stretching of fibers or the interfibrillar and interfiber sliding. These can account for the significant difference with the maximum strain in the transverse direction, which can have values up to 4. These values for the three layers in the pouch skin reflect well the ability of the material to extend considerably, without involving elastic stretching of the fibrils and sliding. Indeed, the heel transition strain for transverse samples in the bulk region of the gular sac is in fair agreement with these results (see, for example, Fig. 12b). It is interesting that the interior *stratum corneum* unfolds less than the exterior layer. This can be explained by the non-planar geometry of the sac, which is curved inward. The curvature of collagen suggests that the total unfolding of the collagen fibers in the middle layer occurs after the elastic deformation of the surrounding strata is ini-

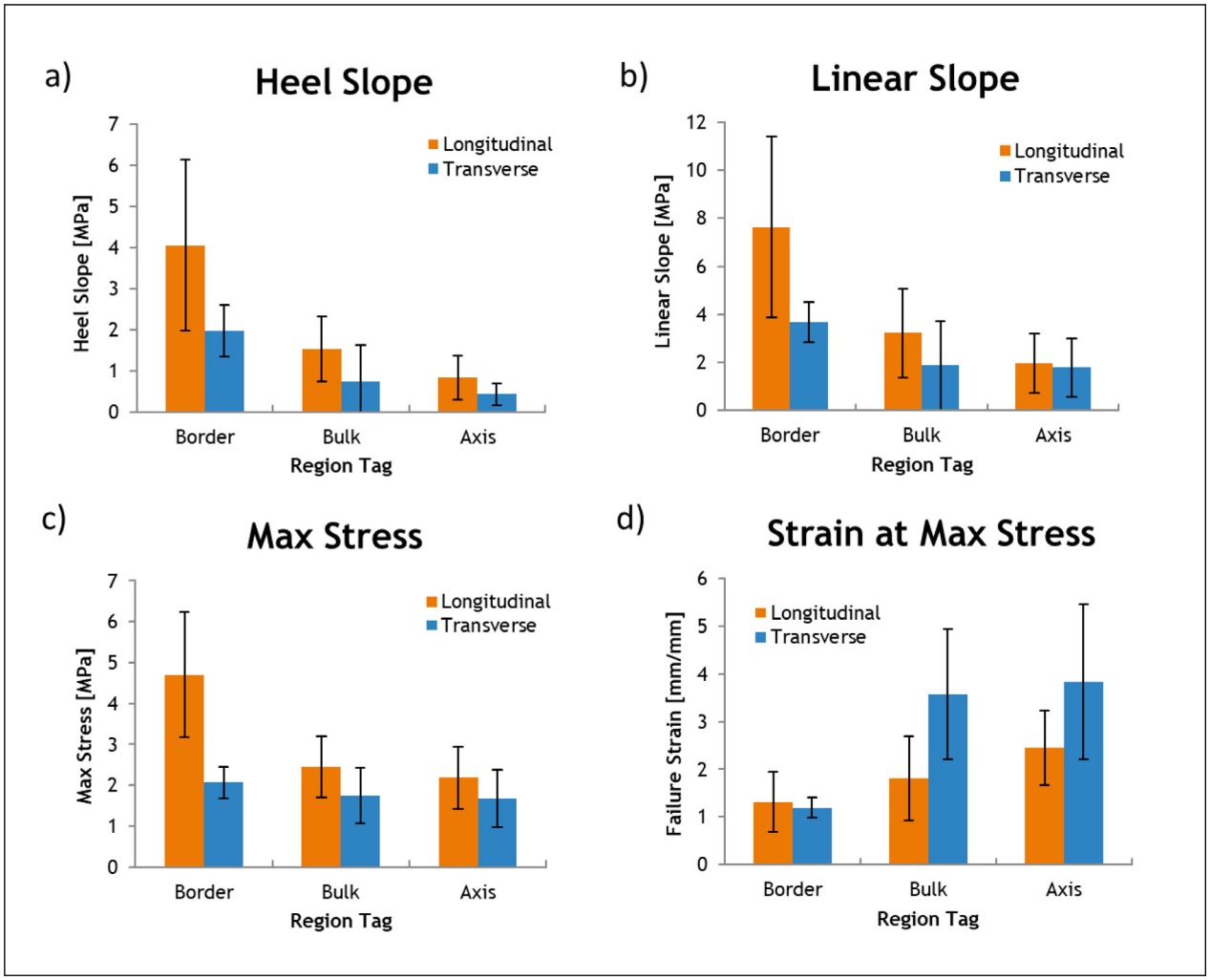

Fig. 13. Tensile response parameters reinterpreting the dorsoventral groupings of Fig. 12. (a-b) Tangent moduli for the heel and linear regions decrease towards the pouch's axis of symmetry. (c) Maximum stress generally decreases towards the axis of symmetry of pouch for longitudinally oriented specimens. Transverse samples exhibit less dependence to dorsoventral locations for this parameter. (d) Strain at the maximum stress increases towards the pouch axis of symmetry for both testing orientations.

Table 2
Calculated average values with standard deviation of the configurational strain due to unfolding of the "M" shapes in the inner and outer strata corneum (see Fig. 10) and of the wavy collagen fibers in the inner layer (see Figs. 4 and 5), taken in the transverse direction.

Layer	$\varepsilon^{conf_{unfold}}$
Interior stratum corneum	0.68 ± 0.01
Middle layer (collagen)	1.07 ± 0.14
Exterior stratum corneum	0.84 ± 0.13

tiated. However, because this process takes place at a much smaller scale, and within a tri-dimensional network containing complex interactions, it is more difficult to expand on the stretchability by fiber unfolding at this level.

Accurate calculations of the configurational strain by rotation (realignment) are more challenging, since they require further knowledge of the tri-dimensional arrangement of the collagenous network, and of the kinematics of rotation associated with it. For the longitudinal direction, the configurational component of the interior and exterior layers disappears, as shown in the schematic in Fig. 14b. As such, assuming full reversibility of the deformation, the stretchability of the gular sac along this orientation (perpendicular to the grooves) is directly limited by the intrinsic elasticity of the interior and exterior layers, as the stress-strain curves suggest. Overall, the tissue gains its remarkable ability to deform because of groove-like structures at two different length scales, *i.e.*, the macroscale and the microscale in the exterior and interior layers. Low stresses are required to reach a large and reversible deformation, without sustaining any damage.

3.6. Constitutive description of gular sac tissue

Starting with the classic contribution by Lanir and Fung [20], there have been many proposals for constitutive descriptions of the deformation of skin [16,20–31] with different levels of complexity and incorporating increasing insights into the physical mechanisms. These models can be classified into three groups [32]:

Phenomenological models, which are essentially mathematical expressions tracking the trajectory of stress versus strain. Many of these were initially developed for polymers and extended to the dermis. The best known are the Ogden [33], Mooney-Rivlin [34,35], and Fung [36] models.

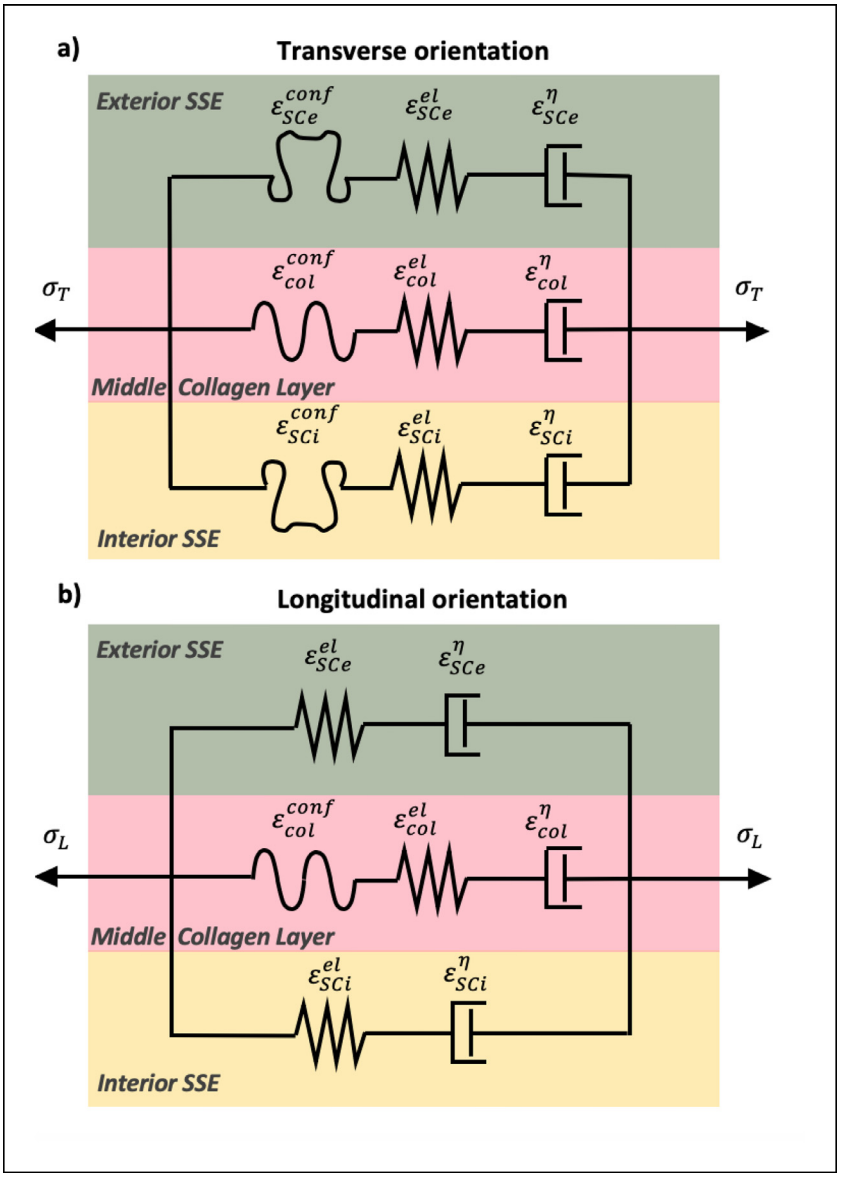

Fig. 14. Rheological models illustrating the distributions of strains for each layer of the gular sac, with contributions of the configurational strain imposed by the geometry and structural arrangement of each component, in the a) transverse direction and b) longitudinal direction. In the longitudinal orientation, the folds do not participate to the deformation and the configurational component disappears.

Semi-structural models incorporating anisotropy through differences in mechanical response depending on orientation. The approach from Lanir [37], Arruda-Boyce [38] and its derivatives [39–41] are good examples, as is the model developed by Sherman et al. [16].

Structural models with fiber dispersion. These models incorporate the dependence of fiber density and waviness on orientation and, in most cases, consider interfibrillar and/or interfiber shear beyond a specific stress or strain. In this sense, they are considerably more realistic; on the other hand, the number of parameters increases. Gasser et al.[42,43]. developed a model for arterial walls, but this model can be expanded to the dermis. Other models were also proposed [37,44,45]. Limbert [45] first incorporated inter fiber and fiber-matrix shear into the deformation of skin. They applied their model to experimental results by Lanir and Fung [20] with stretches as high as 1.9 in the direction perpendicular to the Langer lines. Pissarenko et al. [14] developed a model with interfibrillar shear and straightening and reorientation of the fibers that aligned well with their experimental uniaxial tensile tests on porcine skin. Annaidh et al.[11]. determined the anisotropy of human skin and established the contribution of fiber dispersion to the anisotropic behavior of skin. Jor et al. [46] used confocal imaging of cross-sections of pig skin to measure the angular distribution of collagen fibers. They made an important observation: fibers are not only dispersed in the plane of the skin, but also occur at angles of ~45° to the surface. This tridimensional distribution with an out-of-plane component in the undeformed dermis was further investigated by Pissarenko et al. [14].

However, none of these constitutive models have been applied to the extreme anisotropy and maximum deformation of the gular sac. As shown earlier, there are additional mechanisms operating. Thus, a constitutive description is proposed here for the configurational component of strain in the central, collagenous layer. It incorporates the basic elements of a recent constitutive model

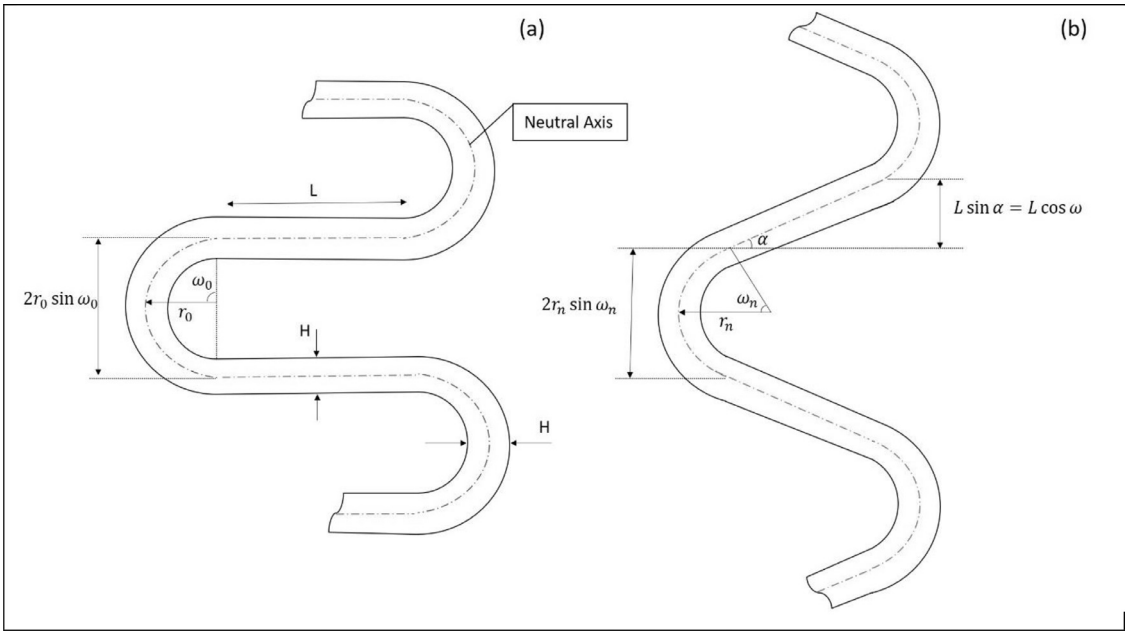

Fig. 15. Collagen fiber configuration based on Fig. 6a, consisting of adjoining circular and straight segments; (a) initial configuration; (b) configuration at time t_n. The included angle ω decreases from its initial value ω_o to a final value equal to 0. Straight segments remain straight and have a constant length L.

for pig skin [14]. The much-increased maximum strain, especially in the transverse orientation, coupled with the essential unfolding of the collagen fibers are evidenced in Fig. 6a. A simple predictive picture that captures the essential features of this structure is shown in Fig. 15. It departs from conventional constitutive models for skin in that there are straight segments which connect circular segments. This stratagem enables much larger maximum strains. Fig. 15b shows the contributions of the increase in radius of circular segments and rotation of straight segments. The total strain (stretch ratio) can be quantified through the kinematic relationships. The opening of the circular segments through interfibrillar sliding results in the increase in r, the radius of the neutral axis; concomitantly, the angle ω (defined in Fig. 15a) decreases from its initial value ω_o. Fig. 15b shows that the angle α is related to ω by:

$$\alpha = \frac{\pi}{2} - \omega. \tag{3}$$

The constitutive model adopted here, which captures the elastic and viscoelastic components of the deformation, is based on a number of simplifying assumptions. It does not incorporate the rotation of the circular segments, only their opening; the straight segments remain straight and their rotation toward the tensile axis is dictated by the angular change at the extremity of the circular segments, to which they are rigidly attached. The effective nominal strain at stage n is expressed as:

$$\varepsilon = \frac{Lcos\omega_n + 2r_n sin\omega_n - 2r_0 sin\omega_0}{2r_0 sin\omega_0}, \tag{4}$$

where the dimensions of L and r are defined in Figs. 15 and 16.

Fig. 17 shows the effect of the ratio L/r_o on the maximum strain achievable for different values of the initial angle ω_0. This maximum strain reaches values of 4 for $\omega_o = \pi/2$. Since the length of the curved segment is constant, from Fig. 16 it follows that:

$$r_o\omega_o = r_n\omega_n. \tag{5}$$

The driving force to effect this change in configuration is interfibrillar sliding, which is maximum at $\pm\omega_n/2$, the stiffness of the fibers is dictated by the fiber modulus E_f. The model presented here assumes $r_o \gg H$, the fiber diameter, and that, as a consequence, all fibrils have the same length; this ensures the constant coupling of α and ω (Fig. 16). Interfibrillar sliding is shown by the displacements δ_k of the k^{th} fibril in Fig. 16a. The summation of the displacement provides an estimate of δ_t.

It is considered that the deformation process of any fibril in the bundle is equivalent to the deformation of the neutral fibril, with an initial radius of curvature r_n and opening angle ω_n. The contribution of all the fibrils is then obtained by summation of the bending energies. The study of the deformation of a single fibril can be further reduced to the analysis of one semi-circular portion of the S-shape, using a one-dimensional curved beam analogy. It is also convenient to introduce the fibril curvature $\rho_n = 1/r_n$.

We consider two successive deformation states, denoted by $(t-1)$ and t. The total internal energy of the structure is the sum of the bending energies of all the fibrils in the fiber, the increment in bending energy of the fibril ΔU_{Bf} is expressed as follows:

$$\Delta U_{Bf} = \frac{1}{2}\int_{-\omega_n}^{\omega_n} E_f I \left(\rho_n^t - \rho_n^{t-1}\right)^2 r_0 d\theta_n, \tag{6}$$

where $\Delta\rho$ is the change in curvature ($=1/\Delta r$, the change in radius) which is a function of the opening angle ω_n, I is the moment of inertia of the fibrils, and θ_n is a variable angle limited by the opening angle ω_n ($\theta_n \le \omega_n$). The total shear energy is given by:

$$\Delta U_{sh}^k = \int_0^{\omega_n} G_m \Delta\gamma_k^2 \; r_0 d_f d_{int} \; d\theta_n, \tag{7}$$

where G_m is the shear modulus for interfibrillar shear.

The total energy is the sum of the two, taking into account the number of fibrils in a fiber, n_f:

$$\Delta U = n_f \Delta U_B^f + \left(n_f - 1\right)\Delta U_{sh}^k \tag{8}$$

ΔU incorporates both the stiffness of fibrils and resistance to interfibrillar shear. The external force providing deformation is shown in Fig. 16 as F_p. The final value, upon rectification, is F_f. The principle of complementary virtual work is used now: the variation in external work $\delta W_e = \Delta F_p \delta u_x$ is equal to the variation of the

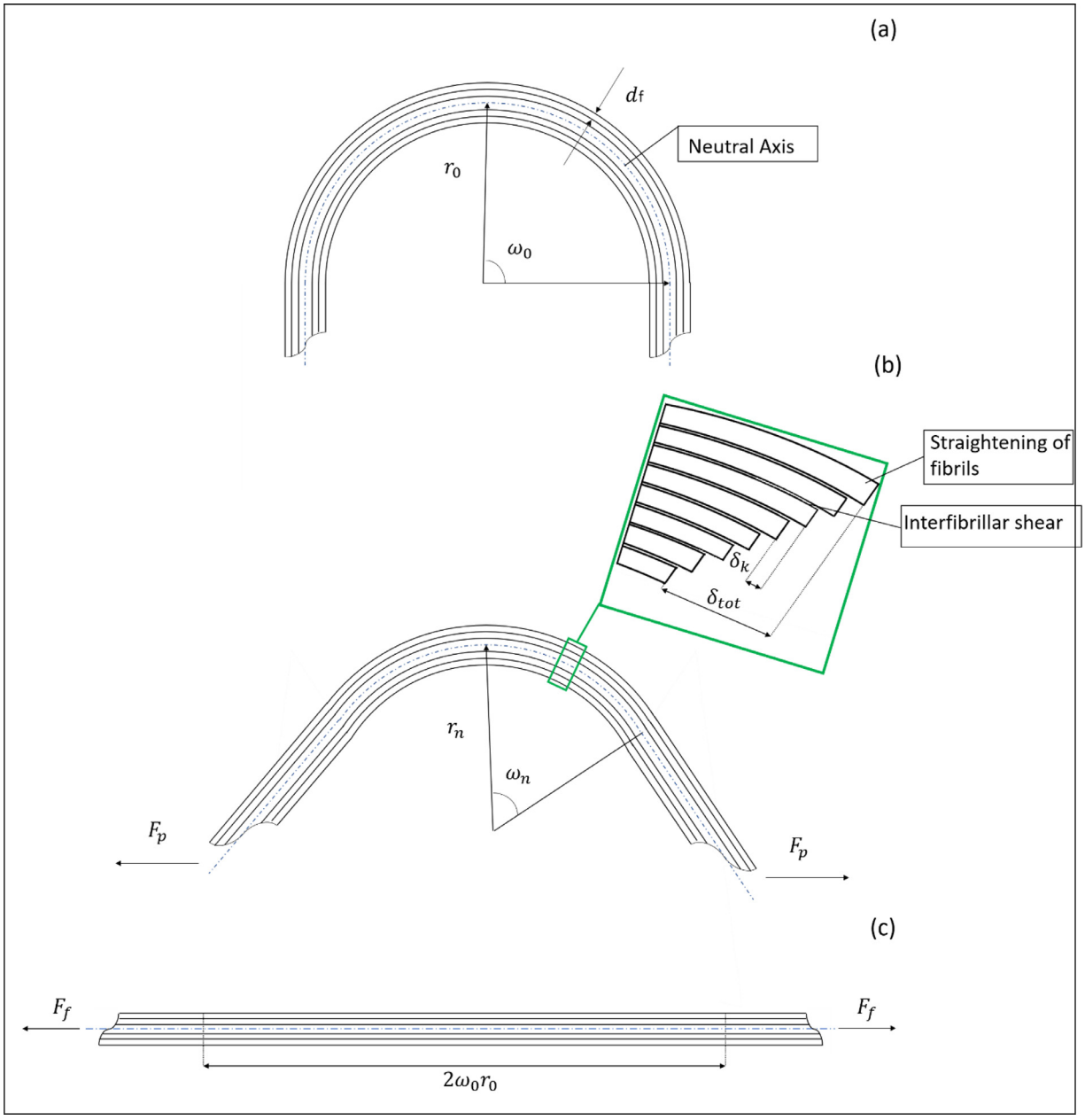

Fig. 16. Interfibrillar sliding leading to increase in radius of the circular segments from (a) r_o to (b) r_n, and finally to (c) rectification ($r = \infty$); notice that the straight segments only rotate and that rotation is determined by the change in included angle ω. The external force F_n increases from 0 to the final value F_f.

internal energy $\delta(\Delta U)$. Hence, the increment of force ΔF_p is obtained by isolating the factor in front of δu_x in the expression of $\delta(\Delta U)$:

$$\frac{\Delta F_p}{\Delta \rho} = \left[\frac{1}{2} n_f E_f I L_f + \left(n_f - 1\right)\frac{G_m L_f^3}{96}\frac{d_f\left(d_f + d_{int}\right)^2}{d_{int}}\right] \times \frac{{\rho_n}^2}{4(\omega_n \cos(\omega_n) - \sin(\omega_n))}. \quad (9)$$

I is the moment of inertia and is defined, for a circular cross section with diameter d_f, as $I = \pi d_f^4/64$. L_f, the length of the circular section at the neutral axis, is equal to $2r_o\omega_o$. Integration of the two sides provides:

$$\partial F = A \int_{\rho_0}^{0} \frac{\rho^2}{[2\pi\rho\cos(2\pi\rho) - \sin(2\pi\rho)]}\partial\rho, \quad (10)$$

where the parameter A is:

$$A = \left(\frac{1}{2} n_f E_f I L_f\right) + \left[\left(n_f - 1\right)\frac{G_m L_f^3}{96}\frac{d_f\left(d_f + d_{int}\right)^2}{d_{int}}\right]. \quad (11)$$

The stress is obtained from F by dividing the force by the cross-sectional area of the fiber, $\pi H^2/4$, as:

$$\sigma = \frac{4A\int_{\rho_0}^{0} \frac{\rho^2}{[2\pi\rho\cos(2\pi\rho) - \sin(2\pi\rho)]}\partial\rho}{\pi H^2}. \quad (12)$$

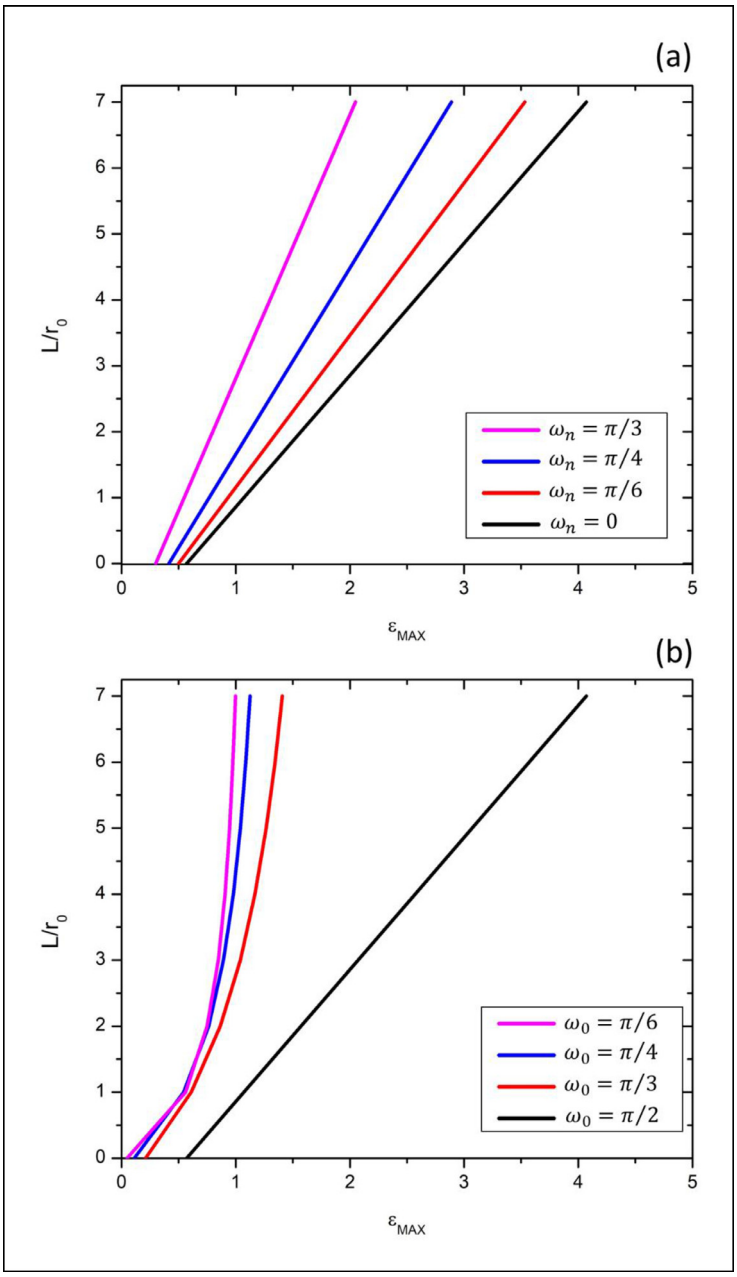

Fig. 17. (a) Maximum strain at different values of ω_n as a function of L/r_o for $\omega_o = \pi/2$; (b) Maximum strain at different values of ω_o as a function of L/r_o for $\omega_n = \pi/2$.

Similarly, the strain can be extracted from the values of ρ, as is obtained by generalizing Eq. (4):

$$\varepsilon = \frac{L\cos(r_0\omega_o\rho) + 2\rho^{-1}\sin(r_0\omega_o\rho) - L\cos(\omega_0) - 2r_0\sin(\omega_0)}{L\cos(\omega_0) + 2r_0\sin(\omega_0)} \tag{13}$$

The parameters used in the current model are based on measurements made in the previous sections and are reported in Table 3. However, they should only be construed as approximate values.

Fig. 17 shows the maximum strains that can be reached using the straight segments between circular segments. The maximum strains at different final values of ω_n for an initial value $\omega_o = \pi/2$ are shown in Fig. 17a. In Fig. 17b, the initial value of ω_o was varied and the specimen was stretched to full rectification. It is clear

Table 3
Structural features of collagen fibers and fibrils for the pelican pouch. Values are approximate and are averages from measurements made and reported in this study and from Pissarenko et al. [14].

Parameter	Mean value
Fiber radius of curvature r_n^0	$4\,\mu m$
Fiber density D_f	0.7
Initial fiber opening angle ω_n^0	45°
Fiber thickness H	$2\ \mu m$
Fibril density per fiber D_f	0.7
Fibril diameter d_f	$150\,nm$
Straight segment length L	$20-30\ \mu m$
Collagen fibril stiffness E_f	30–1570 MPa (800 MPa)
Fibril interspace shear modulus, G_m	10 MPa
Fibrils per fiber, n_f	150
Radius of circular segments, r_o	4 μm

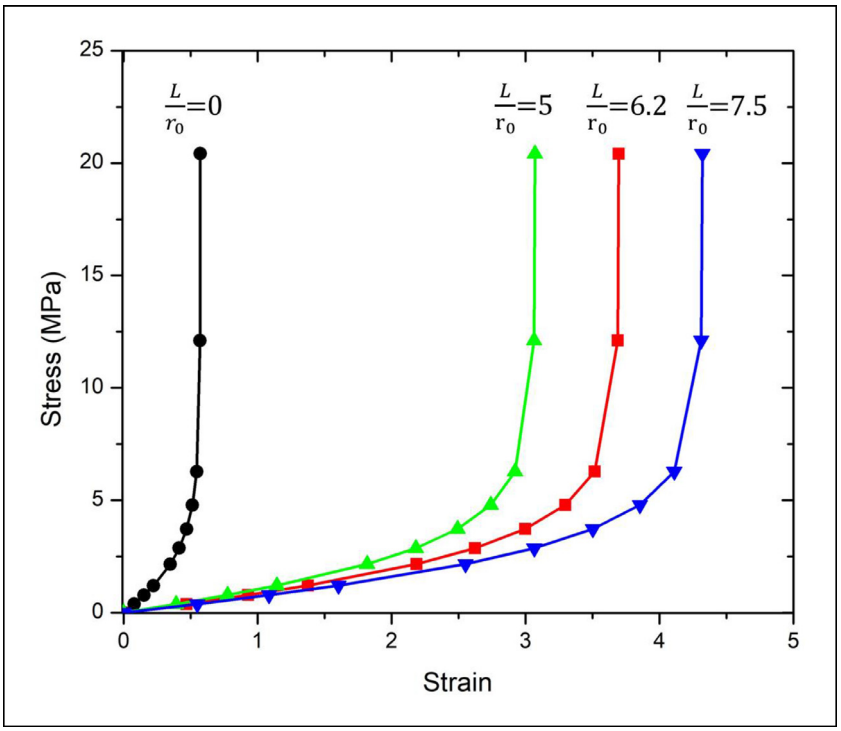

Fig. 18. Calculated stress vs. strain curves for gular skin using current constitutive equation for different values of L/r_o. As the ratio increases, so does the maximum strain. When L/r_o =0, the response is characteristic of porcine skin (Pissarenko et al. [14]).

that ε_{max} increases with a decreasing initial ω_o as well as with the ratio L_f/r_o. Hence, our definition of strain addresses the high maximum strains exhibited by the pelican gular sac in a satisfactory manner. The stress-strain response of the tissue is presented in graphic form in Fig. 18. The values were obtained by integrating Eq. (12) from the initial value of $\rho_o = 0.25\ \mu m^{-1}$ to arbitrarily chosen intermediate values. Thus, the calculations show intervals. The response is in clear agreement with the experimental results. It should be mentioned that the only parameter that was chosen in an arbitrary manner was the elastic modulus of the fibrils, which is listed to be in the range of 30–1570 MPa; an average value of 800 MPa was chosen. In Fig. 18, the black curve for which $L_f = 0$, represents a normal skin as modeled by Pissarenko et al. [14]. The addition of the straight segments increases the maximum strain significantly, while the curves retain their characteristic shape. Thus, this constitutive equation represents the gradual transition from a normal mammal skin (porcine) to the gular sac with its much higher extensibility.

4. Conclusions

The feeding strategy of the brown pelican, which consists of diving and capturing the prey in the sac under the water, puts particular requirements on the pouch skin. It has to stretch laterally considerably, to accommodate the prey, without too much longitudinal strain to avoid the formation of a 'hanging' sac. The pelican only swallows the prey (fish) after exiting the water and expelling the excess liquid from the sac. This research has revealed the detailed structure of the pelican gular sac through characterization and mechanical testing. Based on this study, the following conclusions can be drawn:

1 The structure of the gular sac (pouch) skin consists of a middle layer comprised of collagen sandwiched between two layers of squamous tissue, one internal and one external. The collagen fibrils (with a bimodal distribution of diameters with maxima at 100 and 170 nm) are organized into fibers with diameters of ~2 μm. These fibers form a wavy pattern that is three-dimensional. Upon rotation, straightening, stretching, and sliding, they provide a maximum strain that is on the order of unity in the longitudinal direction. This mechanism is essentially the same as that observed for the ductility of rabbit and pig skin [10,15,16]. In the transverse direction, the unfolding of the corrugations in the interior and exterior layers provides the additional strain required for the maximum value, which approaches 4.
2 Grooves run longitudinally along the sac in a similar manner to rorqual whales. This is a clear example of evolutionary convergence with the unfolding of the grooves providing additional strain. The strains calculated from the microstructural observations are found to be in good agreement with the maximum strains measured in tensile tests on the pouch.
3 The tensile stress-strain curves exhibit considerable anisotropy in the pouch of adult pelicans, with the maximum strain in the transverse direction being approximately three to four times the one in the longitudinal direction. However, for the youngest birds, the transverse and longitudinal results were found to be very similar.
4 The pouch shows a clear gradient in mechanical properties from the axis, bulk to the region close to the beak. Such a graded transition optimizes the damage tolerance of the pouch by providing a failure avoidance strategy between beak and pouch.
5 The pouch skin in both longitudinal and transverse directions exhibits, from border to axis, a decrease in maximum stress and elastic modulus in the heel and linear regions of tension curves and an increase in failure strain. This trend supports the hypothesis that a specimen's dorsoventral location influences the properties associated with it.

6 The skin near the beak, in the 'border' region, is stiffer and stronger in order to ensure continuity in mechanical behavior and maintain a tight connection to the stiff beak.
7 A constitutive equation for the middle layer is proposed and tested using experimentally obtained material parameters for the gular sac. It consists of semi-circular (akin to Pissarenko et al. [14]) and straight segments (our innovation) forming the fiber. Upon tensile extension, the circular segment radii increase and the straight segments rotate toward the tensile axis. The predictions of the constitutive equation agree well with the experimental results and strains up to 4 are obtained using adjustable ratios between the circular segment radii and straight segment lengths.

Declaration of Competing Interest

The authors declare that they have no known competing financial interests or personal relationships that could have appeared to influence the work reported in this paper.

Acknowledgments

This work was funded by a Multi-University Research Initiative (grant no. AFOSR-FA9550–15–1–0009) from the Air Force Office of Scientific Research to the University of California Riverside, through subcontracts to the University of California, San Diego (MAM) and the University of California, Berkeley (ROR). MAM also acknowledges partial funding from the National Science Foundation through the Division of Mechanics of Materials and Structures (Grant numbers 1926353 and 1926361). We thank Kaylin Ackerson, Alexandria Mena and Judy Leger from San Diego Sea World and Philip Unitt from San Diego Natural History Museum for providing the pelican specimens. A very special gratitude is owed to Alex Li, who provided valuable help by performing the numerical integration which enabled obtaining the stress vs. strain curve in the constitutive model.

Supplementary materials

Supplementary material associated with this article can be found, in the online version, at doi:10.1016/j.actbio.2020.10.008.

References

[1] D.J. Field, S.C. Lin, M. Ben-Zvi, J.A. Goldbogen, R.E. Shadwick, Convergent evolution driven by similar feeding mechanics in balaenopterid whales and pelicans, Anat. Rec. 294 (2011) 1273–1282.
[2] R.W. Schreiber, G.E. Woolfenden, W.E. Curtsinger, Prey capture by the Brown Pelican, Auk (1975) 649–654.
[3] J. Potvin, J.A. Goldbogen, R.E. Shadwick, Passive versus active engulfment: verdict from trajectory simulations of lunge-feeding fin whales Balaenoptera physalus, J. R. Soc. Interface. 6 (2009) 1005–1025.
[4] N. Reuge, F.M. Schmidt, Y. Le Maoult, M. Rachik, F. Abbe, Elastomer biaxial characterization using bubble inflation technique. I: experimental investigations, Polym. Eng. Sci. 41 (2001) 522–531.
[5] J. Schindelin, I. Arganda-Carreras, E. Frise, V. Kaynig, M. Longair, T. Pietzsch, S. Preibisch, C. Rueden, S. Saalfeld, B. Schmid, J.Y. Tinevez, Fiji: an open-source platform for biological-image analysis, Nat. Methods 9 (2012) 676–682.
[6] JMP®, Version 14.1.0. SAS Institute Inc., Cary, NC, 1989–2019.
[7] L.S. Orton, P.F. Brodie, Engulfing mechanics of fin whales, Can. J. Zool. (Revue Canadienne De Zoologie). 65 (1987) 2898–2907.
[8] T.D. Williams, P.Q. Gawlowski, D.M. Strickland, Surgical repair of the gular sac of the brown pelican (Pelecanus occidentalis), J. Zoo Anim. Med. 19 (1988) 122–125.
[9] K. Bircher, M. Zündel, M. Pensalfini, A.E. Ehret, E. Mazza, Tear resistance of soft collagenous tissues, Nature Comm 10 (2019) 1–13.
[10] A. Pissarenko, W. Yang, H. Quan, K.A. Brown, A. Williams, W. Proud, M.A. Meyers, Tensile behavior and structural characterization of pig dermis, Acta Biomater. 86 (2019) 77–95.
[11] A.N. Annaidh, K. Bruyere, M. Destrade, M.D. Gilchrist, C. Maurini, M. Otténio, G. Saccomandi, Automated estimation of collagen fibre dispersion in the dermis and its contribution to the anisotropic behaviour of skin, Ann. Biomed. Eng. 40 (2012) 1666–1678.
[12] W.D. Meador, G.P. Sugerman, H.M. Story, A.W. Seifert, M.R. Bersi, A.B. Tepole, M.K. Rausch, The regional-dependent biaxial behavior of young and aged mouse skin: a detailed histomechanical characterization, residual strain analysis, and constitutive model, Acta Biomater. 101 (2020) 403–413.
[13] R. Rezakhaniha, A. Agianniotis, J.T.C. Schrauwen, A. Griffa, D. Sage, C.V. Bouten, F.N. Van De Vosse, M. Unser, N. Stergiopulos, Experimental investigation of collagen waviness and orientation in the arterial adventitia using confocal laser scanning microscopy, Biomech. Model Mechanobiol. 11 (2012) 461–473.
[14] A. Pissarenko, C.J. Ruestes, M.A. Meyers, Constitutive description of skin dermis: through analytical continuum and coarse-grained approaches for multi-scale understanding, Acta Biomater. 106 (2020) 208–224.
[15] W. Yang, V.R. Sherman, B. Gludovatz, E. Schaible, P. Stewart, R.O. Ritchie, M.A. Meyers, On the tear resistance of skin, Nat. Commun. 6 (2015) 6649.
[16] V.R. Sherman, Y. Tang, S. Zhao, W. Yang, M.A. Meyers, Structural characterization and viscoelastic constitutive modeling of skin, Acta Biomater. 53 (2017) 460–469.
[17] W. Yang, M.A. Meyers, R.O. Ritchie, Structural architectures with toughening mechanisms in Nature: a review of the materials science of Type-I collagenous materials, Prog. Mater. Sci. 103 (2019) 425–483.
[18] T.W. Herod, N.C. Chambers, S.P. Veres, Collagen fibrils in functionally distinct tendon rupture and fatigue loading, Acta Biomater. 42 (2016) 296–307.
[19] G. Arnqvist, Brown pelican foraging success related to age and height of dive, Condor 94 (1992) 521–522.
[20] Y. Lanir, Y.C. Fung, Two-dimensional mechanical properties of rabbit skin – II Experimental results, J. Biomech. 7 (1974) 171–182.
[21] G. Limbert, Mathematical and computational modelling of skin biophysics: a review, Proc. R. Soc. A Math. Phys. Eng. Sci (2017) 473.
[22] S.D. Łagan, A. Liber-Kneć, Experimental testing and constitutive modeling of the mechanical properties of the swine skin tissue, Acta Bioeng. Biomech. 19 (2017) 93–102.
[23] P.A.L.S. Martins, R.M.N. Jorge, A.J.M. Ferreira, A Comparative Study of Several Material Models for Prediction of Hyperelastic Properties: application to Silicone-Rubber and Soft Tissues, Strain 42 (2006) 135–147.
[24] G. Limbert, J. Middleton, A transversely isotropic viscohyperelastic material: application to the modeling of biological soft connective tissues, Int. J. Solids Struct. 41 (2004) 4237–4260.
[25] R.B. Groves, S.A. Coulman, J.C. Birchall, S.L. Evans, An anisotropic, hyperelastic model for skin: experimental measurements, finite element modelling and identification of parameters for human and murine skin, J. Mech. Behav. Biomed. Mater. 18 (2013) 167–180.
[26] D. Pond, A. McBride, L. Davids, B.D. Reddy, G. Limbert, Microstructurally-based constitutive modeling of the skin – Linking intrinsic ageing to microstructural parameters. (2017) 1–32. Available at: http://arxiv.org/abs/1709.03752.
[27] J.W.Y. Jor, P.M.F. Nielsen, M.P. Nash, P.J. Hunter, Modelling collagen fibre orientation in porcine skin based upon confocal laser scanning microscopy, Skin Res. Technol. 17 (2011) 149–159.
[28] Y. Gao, A.M. Waas, J.A. Faulkner, T.Y. Kostrominova, A.S. Wineman, Micromechanical modeling of the epimysium of the skeletal muscles, J. Biomech. 41 (2008) 1–10.
[29] J.W.Y. Jor, M.P. Nash, P.M.F. Nielsen, P.J. Hunter, Estimating material parameters of a structurally based constitutive relation for skin mechanics, Biomech. Model. Mechanobiol 10 (2011) 767–778.
[30] A. Ni Annaidh, K. Bruyere, M. Destrade, M.D. Gilchrist, M. Ottenio, Characterization of the anisotropic mechanical properties of excised human skin, J. Mech. Behav. Biomed. Mater. 5 (2012) 139–148.
[31] H. Joodaki, H.M.B. Panzer, Skin mechanical properties and modeling: a review, Proc. Inst. Mech. Eng. H 232 (2018) 323–343.
[32] A. Pissarenko, M.A. Meyers, The materials science of skin: analysis, characterization, and modeling, Prog. Mater. Sci. 110 (2020) 100634.
[33] R.W. Ogden, Large Deformation Isotropic Elasticity - On the Correlation of Theory and Experiment for Incompressible Rubberlike Solids, Proc. R. Soc. A Math. Phys. Eng. Sci 326 (1972) 565–584, doi:10.1098/rspa.1972.0026.
[34] M. Mooney, A Theory of Large Elastic Deformation, J. Appl. Phys. 11 (1940) 582–592, doi:10.1063/1.1712836.
[35] R.S. Rivlin, Large Elastic Deformations of Isotropic Materials. IV. Further Developments of the General Theory, Philos. Trans. R. Soc. A Math. Phys. Eng. Sci. 241 (1948) 379–397, doi:10.1098/rsta.1948.0024.
[36] Y.C. Fung, Elasticity of soft tissues in simple elongation, Am. J. Physiol 213 (1967) 1532–1544, doi:10.1152/ajplegacy.1967.213.6.1532.
[37] Y. Lanir, Constitutive equations for fibrous connective tissues, J. Biomech. 16 (1983) 1–12 Crossref, PubMed, ISI, Google Scholar, doi:10.1016/0021-9290(83)90041-6.
[38] E.M. Arruda, M.C. Boyce, A three-dimensional constitutive model for the large strech behavior fo rubber elastic materials, J. Mech. Phys. Solids 41 (1993) 389–412, doi:10.1016/j.commatsci.2011.10.026.
[39] E. Kuhl, K. Garikipati, E.M. Arruda, K. Grosh, Remodeling of biological tissue: mechanically induced reorientation of a transversely isotropic chain network, J. Mech. Phys. Solids. 53 (2005) 1552–1573, doi:10.1016/j.jmps.2005.03.002.
[40] J.S. Bergström, M.C. Boyce, Constitutive modeling of the time-dependent and cyclic loading of elastomers and application to soft biological tissues, Mech. Mater 33 (2001) 523–530, doi:10.1016/S0167-6636(01)00070-9.
[41] J.E. Bischoff, E.M. Arruda, K. Grosh, A rheological network model for the continuum anisotropic and viscoelastic behavior of soft tissue, Biomech. Model. Mechanobiol 3 (2004) 56–65, doi:10.1007/s10237-004-0049-4.

[42] T.C. Gasser, R.W. Ogden, G.A. Holzapfel, Hyperelastic modelling of arterial layers with distributed collagen fibre orientations, J. R. Soc. Interface. 3 (2006) 15–35, doi:10.1098/rsif.2005.0073.
[43] G.A. Holzapfel, R.W. Ogden, S. Sherifova, On fibre dispersion modelling of soft biological tissues: a review, Proc. R. Soc. A Math. Phys. Eng. Sci. 475 (2019), doi:10.1098/rspa.2018.0736.
[44] O. Lokshin, Y. Lanir, Viscoelasticity and Preconditioning of Rat Skin Under Uniaxial Stretch: microstructural Constitutive Characterization, J. Biomech. Eng. 131 (2009) 31009, doi:10.1115/1.3049479.
[45] G. Limbert, A mesostructurally-based anisotropic continuum model for biological soft tissues-Decoupled invariant formulation, J. Mech. Behav. Biomed. Mater. 4 (2011) 1637–1657, doi:10.1016/j.jmbbm.2011.07.016.
[46] J.W.Y. Jor, M.D. Parker, A.J. Taberner, M.P. Nash, P.M. Nielsen, Computational and Experimental Characterization of Skin Mechanics: identifying Current Challenges and Future Directions, Rev. Syst. Biol. Med 5 (2013) 539–556.